JGR Oceans

RESEARCH ARTICLE
10.1029/2020JC016863

Mean and Seasonal Circulation of the Eastern Chukchi Sea From Moored Timeseries in 2013–2014

Fei Tian[1], Robert S. Pickart[2], Peigen Lin[2], Astrid Pacini[2], G. W. K. Moore[3], Phyllis Stabeno[4], Thomas Weingartner[5], Motoyo Itoh[6], Takashi Kikuchi[6], Elizabeth Dobbins[5], Shaun Bell[4,7], Rebecca A. Woodgate[8], Seth L. Danielson[5], and Zhaomin Wang[1]

[1]International Polar Environmental Research Laboratory, College of Oceanography, Hohai University, Nanjing, China, [2]Woods Hole Oceanographic Institution, Woods Hole, MA, USA, [3]Department of Physics, University of Toronto, Toronto, ON, Canada, [4]Pacific Marine Environmental Laboratory, National Oceanic and Atmospheric Administration, Seattle, WA, USA, [5]College of Fisheries and Ocean Sciences, University of Alaska, Fairbanks, AK, USA, [6]Institute of Observational Research for Global Change, Japan Agency for Marine-Earth Science and Technology, Yokosuka, Japan, [7]Joint Institute for the Study of the Atmosphere and Oceans, University of Washington, Seattle, WA, USA, [8]Applied Physics Laboratory, University of Washington, Seattle, WA, USA

Key Points:

- The appearance of warm water across the Chukchi shelf in spring is dictated by advection, but the appearance of cold water in the fall is not
- Wind mixing from autumn storms brings cold, fresh water to depth on the mid-shelf, but strong stratification prohibits this farther north
- The circulation during the warm and cold months of the year is different in both strength and pattern

Correspondence to:
R. S. Pickart,
rpickart@whoi.edu

Citation:
Tian, F., Pickart, R. S., Lin, P., Pacini, A., Moore, G. W. K., Stabeno, P., et al. (2021). Mean and seasonal circulation of the eastern Chukchi Sea from moored timeseries in 2013–2014. *Journal of Geophysical Research: Oceans*, *126*, e2020JC016863. https://doi.org/10.1029/2020JC016863

Received 7 OCT 2020
Accepted 23 APR 2021

Abstract From late-summer 2013 to late-summer 2014, a total of 20 moorings were maintained on the eastern Chukchi Sea shelf as part of five independent field programs. This provided the opportunity to analyze an extensive set of timeseries to obtain a broad view of the mean and seasonally varying hydrography and circulation over the course of the year. Year-long mean bottom temperatures reflected the presence of the strong coastal circulation pathway, while mean bottom salinities were influenced by polynya/lead activity along the coast. The timing of the warm water appearance in spring/summer is linked to advection along the various flow pathways. The timing of the cold water appearance in fall/winter was not reflective of advection nor related to the time of freeze-up. Near the latitude of Barrow Canyon, the cold water was accompanied by freshening. A one-dimensional mixed-layer model demonstrates that wind mixing, due to synoptic storms, overturns the water column resulting in the appearance of the cold water. The loitering pack ice in the region, together with warm southerly winds, melted ice and provided an intermittent source of fresh water that was mixed to depth according to the model. Farther north, the ambient stratification prohibits wind-driven overturning, hence the cold water arrives from the south. The circulation during the warm and cold months of the year is different in both strength and pattern. Our study highlights the multitude of factors involved in setting the seasonal cycle of hydrography and circulation on the Chukchi shelf.

Plain Language Summary From late-summer 2013 to 2014, a total of 20 moorings were maintained on the eastern Chukchi Sea shelf, north of Bering Strait, as part of five independent field programs. We analyze these data to obtain a broad view of the mean water conditions and circulation, as well as the dominant variability over the course of the year. The year-long mean bottom temperatures reflected the presence of the strong current adjacent to the Alaskan coast, while the mean bottom salinities were influenced by the frequent presence of persistent openings in the sea ice, which result in the formation of salty water when the ice re-freezes. The appearance of warm water across the shelf in spring/summer was mainly dictated by the speed of the water from south to north. However, the appearance of cold water in fall/winter was not reflective of this. Using a simple model, it is demonstrated that storm events mixed cold and fresh surface water to the bottom on the mid-shelf. Farther to the northeast, this does not happen because the water is more stratified, and this prohibits such wind mixing. Finally, it is shown that the circulation during the warm and cold months of the year is different in both strength and pattern.

1. Introduction

Seasonally varying Pacific-origin waters play a critical role in the hydrographic and ecosystem structure of the western Arctic Ocean. Cold water flowing northward through Bering Strait from late-fall through late-spring provides nutrients that fuel primary production (Danielson et al., 2017; Hill & Cota, 2005;

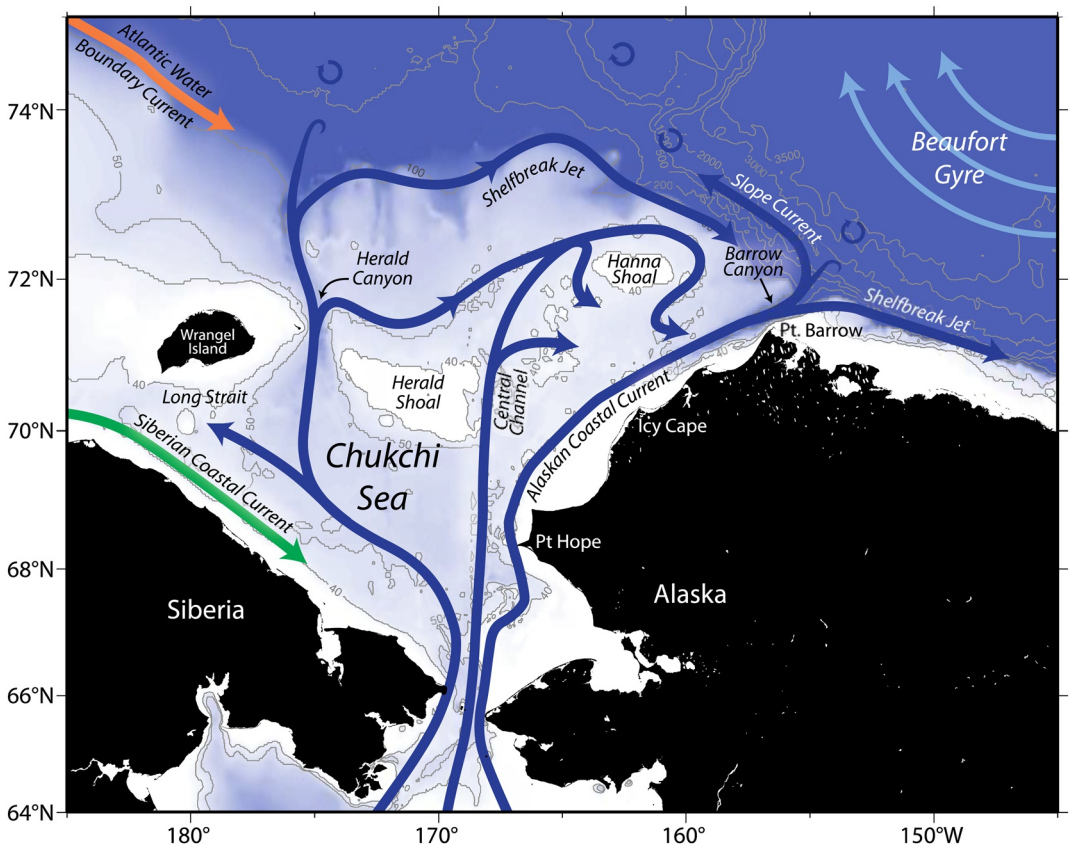

Figure 1. Schematic circulation of the Chukchi Sea (after Corlett & Pickart, 2017), with place names. The bathymetry is from ETOPO-2.

Shimada et al., 2006; Woodgate et al., 2010; Yang, 2006) and ventilate the upper halocline of the Canada Basin (Foukal et al., 2019; Woodgate et al., 2005a). Warm water flowing northward the remainder of the year carries heat that melts pack ice (Brugler et al., 2014; Woodgate et al., 2012) and contributes to the vast freshwater reservoir of the Beaufort Gyre (Pickart et al., 2013; Proshutinsky et al., 2009). During its passage from Bering Strait to the deep Arctic basin, the Pacific-origin water circulates through the wide and shallow Chukchi shelf where it can be significantly modified by ice melt (Weingartner et al., 2005), wind-driven mixing (Woodgate et al., 2005a), and air-sea interaction (Weingartner et al., 1998). Both the magnitude and direction of the flow are strongly influenced by the local wind field, which can alter the residence time of the water on the shelf (Winsor & Chapman, 2004; Woodgate et al., 2005a).

The transport of Pacific water through Bering Strait has increased by ~25% since 2000, and the annual average is now estimated to be 1.0 ± 0.05 Sv (Woodgate, 2018). After leaving the strait the water is topographically steered into three main branches on the Chukchi shelf (Figure 1): the western pathway through Herald Canyon, located between Wrangel Island and Herald Shoal (Coachman et al., 1975; Pickart et al., 2010; Weingartner et al., 2005; Woodgate et al., 2005a); the middle pathway through Central Channel, between Herald and Hanna Shoals (Weingartner et al., 2005); and the eastern pathway that roughly parallels the coast of Alaska (Paquette & Bourke, 1974). Based on detailed shipboard velocity and high frequency radar measurements during the warm months of the year, it has been determined that the middle branch veers to the east around both sides of Hanna Shoal and combines with the coastal pathway, ultimately draining into Barrow Canyon (Fang et al., 2017; Gong & Pickart, 2016; Lin et al., 2019; Pacini et al., 2019; Pickart et al., 2016) (Figure 1). This is consistent as well with mooring, high frequency radar, and drifter data (Stabeno et al., 2018; Weingartner, Fang, et al., 2017). Part of the western pathway is also diverted to the east in the vicinity of Herald Shoal (Pickart et al., 2016; Weingartner et al., 2005) and merges with the middle branch. Finally, a fraction of the western pathway is believed to exit the Chukchi Sea through Long Strait (Woodgate et al., 2005a).

Previous studies of the circulation and hydrography of the Chukchi Sea have revealed strong seasonality in temperature and salinity of the near bottom waters, and rapid response of the flow to wind-forcing. Woodgate et al. (2005a) analyzed a set of year-long timeseries from 12 moorings deployed from autumn 1990 to autumn 1991. They found that, during winter, the small range in temperature-salinity across the shelf implied that brine-driven convective overturning, due to ice formation, transformed most of the water column. This is consistent with the late-spring shipboard data analyzed by Pacini et al. (2019). The largest seasonality in hydrography occurred on the eastern shelf, where warm and fresh water is transported northward during the summer months in the coastal pathway, known as the Alaskan Coastal Current (ACC; Paquette & Bourke, 1974; Wiseman & Rouse, 1980). Woodgate et al. (2005a) found that, averaged over a year, as waters progressed northward across the shelf, temperatures generally decreased while salinities changed comparatively little. Fang et al. (2020) analyzed data from a set of 23 moorings around Hanna Shoal, deployed between 2011 and 2014, and noted a signal of sudden sustained reduction in temperature to near-freezing at the start of winter, and a gradual rebound during the summer months.

Many studies have highlighted the strong impact of wind on the circulation in the vicinity of Bering Strait and on the Chukchi shelf. Woodgate et al. (2005a) concluded that the dominant driver of flow variability across the shelf was wind, although wind-current correlations decreased in the vicinity of the western pathway. Danielson et al. (2014) demonstrated the importance to the regional flow field of both direct Ekman transport and distant wind forcing that triggers propagating continental shelf waves. Northerly wind events readily reverse the typically northward flow through Bering Strait (e.g., Weingartner et al., 2005), and the associated Ekman circulation can divert upper-layer water to the western shelf (Pisareva et al., 2015; Woodgate et al., 2015). The flow through Central Channel and on the northeastern shelf can also be reversed and flow southward during such wind forcing (Danielson et al., 2017; Fang et al., 2017; Pickart et al., 2011; Spall, 2007; Weingartner et al., 1998). Wind-driven upwelling commonly occurs in Barrow Canyon (Aagaard & Roach, 1990; Pisareva et al., 2019; Weingartner, Potter, et al., 2017), which on occasion can flux warm and salty Atlantic Water from the Canada Basin far onto the shelf (Ladd et al., 2016; Woodgate et al., 2005b). Lin et al. (2019) demonstrated that the circulation in the interior portion of the northeast shelf is sensitive to wind stress curl, which drives cyclonic (anti-cyclonic) flow around Hanna Shoal during periods of positive (negative) wind stress curl. Fang et al. (2020) noted that bottom waters flow anticyclonically around the Shoal, with a baroclinic response to forcing from the wind northeast of the shoal. However, they did not observe a clear relationship between low-frequency circulation signals and wind stress curl.

This study presents results from an extensive set of moorings that were deployed in the northeastern Chukchi Sea from late-summer 2013 to 2014 as part of multiple field programs, together with contemporaneous moored measurements from Bering Strait. We take a broad view of the space-time structure and variability of the flow and hydrography on the shelf, reminiscent of the Woodgate et al. (2005a) study that focused on 1990–1991. Conditions have changed considerably during the 23 years between the two sets of measurements, including a longer open water period (Frey et al., 2015), and increased volume, heat, and freshwater fluxes through Bering Strait (Woodgate, 2018). In addition, the moorings considered here are primarily located on the northeastern Chukchi shelf, whereas Woodgate et al.'s (2005a) measurements were spread across the entire shelf with only two moorings in the northeast region, and no moorings north of 71.2°N. Our focus is on the year-long mean and seasonal circulation and water properties, including the role of advection versus local air-sea forcing. The data and analysis techniques are described in Section 2, followed by a presentation of the year-long mean conditions in Section 3. We then consider the seasonal variations in Section 4, including the propagation of hydrographic signals across the shelf and the differences between fast and slow circulation regimes. A summary is presented in Section 5.

2. Data and Methods

2.1. Mooring Data

From a measurement perspective, 2013–2014 was an extraordinary year in that 20 moorings were maintained on the Chukchi shelf as part of five different field programs associated with six different institutions. The spatial coverage of the moorings is shown in Figure 2. Sixteen of the moorings were situated on the northeastern shelf, three were in Bering Strait, and one was roughly 200 km north of the strait near 68°N. The temporal coverage of the data is shown in Figure 3. Nearly all of the records spanned close to a year,

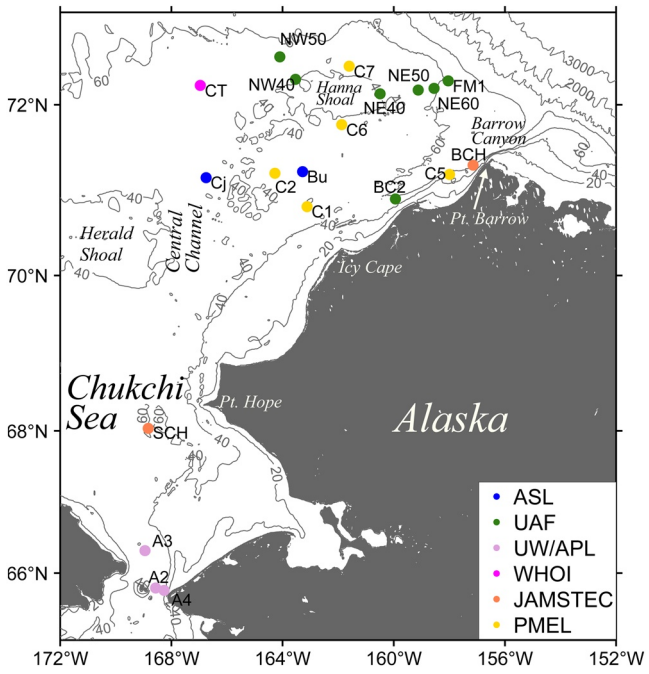

Figure 2. Locations of the moorings used in the study, color-coded by institution (see the legend). The bathymetry is from IBCAO v3.

from September 2013 through August 2014. However, three of the mooring records (Cj, CT, and FM1) were short by 1–3 months. We note that some, but not all, of the moorings analyzed in this study are the same as those discussed in Fang et al. (2020).

All of the moorings were equipped with a single MicroCAT or SeaCAT measuring temperature, conductivity, and pressure near the bottom (1–13 m above the bottom, see Table 1). Eighteen of them contained upward-facing acoustic Doppler current profilers (ADCPs) providing vertical profiles of velocity (the SCH and BCH moorings collected hydrographic information only). Sampling intervals ranged from 15 min to 1 h, and the bin size of the ADCP records ranged from 1 to 10 m. A summary of the mooring information is contained in Table 1. All of the velocity data were de-tided using the T_Tide harmonic analysis toolbox (Pawlowicz et al., 2002), although tidal signals were weak across the shelf (see also Woodgate et al., 2005a). The maximum tidal constituent amplitude (M_2) was 3.8 cm/s, which is small compared to the signals of interest. Small gaps in the timeseries were filled in using Laplacian-spline interpolation.

2.2. Wind and Ice Data

Wind data from the ERA5 climate reanalysis are used in the study, obtained from the European Center for Medium-Range Weather Forecasts (ECMWF, https://rmets.onlinelibrary.wiley.com/doi/10.1002/qj.3803, Hersbach & Dee, 2016). ERA5, which is the follow-on to the ERA-Interim product, is the fifth generation ECMWF atmospheric reanalysis global product and has spatial and temporal resolutions of 0.25° and 1 h, respectively.

The ice concentration product used here is the daily Advanced Microwave Scanning Radiometer 2 (AMSR2) data obtained from the Remote Sensing of Sea Ice Research Group at the University of Bremen (https://seaice.uni-bremen.de/). AMSR2 is the successor to AMSR-E, launched in May 2012. The resolution of the daily data used in this study is 3.125 km.

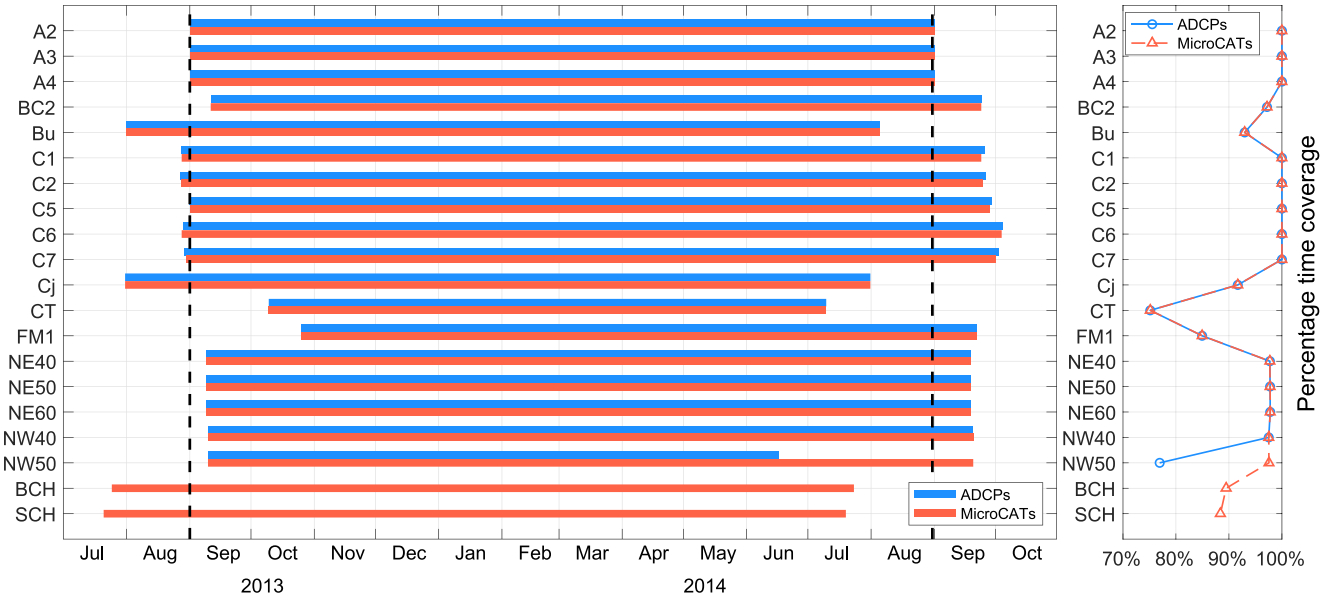

Figure 3. Temporal coverage of the mooring data. The year-long period considered in this study is indicated by the thick dashed lines. The percent data coverage of each instrument over this time period is indicated on the right. See Table 1 for a complete description of the moorings and see Figure 2 for the map of the mooring locations.

Table 1
Mooring Information

ID	Lat (°N)	Lon (°W)	Water depth (m)	Date range (mm/dd/yyyy)	ADCP			MicroCAT		Institution[a]
					Effective range (m)	Sample int. (h)	Vertical res. (m)	Depth (m)	Sample int. (h)	
A2[b,c]	65°47′	168°34′	54	07/06/2013–07/01/2014	1–39	0.5	2	50	1	UW/APL
				07/03/2014–08/31/2014				50	1	
				07/03/2014–08/07/2014	1–39	0.5	2			
				08/07/2014–08/31/2014	1–37	1	4			
A3[b]	66°20′	168°57′	56	07/05/2013–07/02/2014	1–39	0.5	2	45	1	UW/APL
				07/02/2014–08/31/2014	1–39	0.5	2	43	1	
A4[b]	65°45′	168°16′	47	07/06/2013–07/01/2014	1–33	0.5	2	40	1	UW/APL
				07/03/2014–08/31/2014	1–33	0.5	2	40	1	
BCH	71°19′	157°9′	60	07/24/2013–07/23/2014	-	-	-	56	1	JAMSTEC
BC2	70°55′	159°56′	52	09/11/2013–09/23/2014	3–46	0.5	1	51	0.25	UAF
Bu	71°14′	163°17′	46	08/01/2013–08/05/2014	17, 35	0.25	-	38	0.25	ASL
Cj	71°10′	166°45′	47	07/31/2013–07/31/2014	21, 35	0.25	-	40	0.25	ASL
C1	70°50′	163°7′	44	08/27/2013–09/25/2014	4–28	1	4	40	1	PMEL
C2	71°13′	164°17′	43	08/27/2013–09/26/2014	7–37	1	2	39	1	PMEL
C5	71°12′	158°0′	53	08/31/2013–09/29/2014	5–33	1	4	44	1	PMEL
C6	71°47′	161°52′	42	08/28/2013–10/04/2014	13–39	1	2	39	1	PMEL
C7	72°25′	161°36′	42	08/29/2013–10/02/2014	4–32	1	2	41	1	PMEL
CT1	72°13′	166°58′	48	10/09/2013–07/10/2014	8–38	1	5	46	0.25	WHOI
FM1	72°16′	158°2′	67	10/25/2013–09/21/2014	13–53	1	5	61	0.25	UAF
NE40	72°7′	160°30′	41	09/09/2013–09/18/2014	3–37	0.5	1	37	0.25	UAF
NE50	72°10	159°7′	50	09/09/2013–09/18/2014	4–46	0.5	1	46	0.25	UAF
NE60	72°11′	158°33′	57	09/09/2013–09/18/2014	5–53	0.5	1	53	0.25	UAF
NW40	72°17′	163°32′	41	09/10/2013–09/20/2014	3–37	0.5	1	38	0.25	UAF
NW50	72°32′	164°6′	51	09/09/2013–06/16/2014	4–47	0.5	1	47	0.25	UAF
SCH	68°2′	168°50′	61	07/20/2013–07/19/2014	-	-	-	53	1	JAMSTEC

[a]University of Washington Applied Physics Laboratory (UW/APL), Japan Agency for Marine-Earth Science and Technology (JAMSTEC), University of Alaska Fairbanks (UAF), ASL Environmental Sciences, Inc. (ASL), National Oceanic and Atmospheric Administration Pacific Marine Environmental Laboratory (PMEL), Woods Hole Oceanographic Institution (WHOI). [b]Two deployment years were spliced together in order to cover the entire study year, resulting in a small gap at turnaround. ADCPs contained significant errors in the surface bins, so those levels were omitted from the analysis (above 8 m at A2 and above 7 m at A3 and A4). [c]While the MicroCAT operated without incident during the 2014 deployment, the ADCP experienced an error about one month in, which caused it to reset to factory defaults. Portion with 4 m vertical resolution was interpolated to 2 m resolution.

2.3. Heat Fluxes

Heat flux data over the Chukchi shelf are used to force the one-dimensional mixing model (described in Section 2.4) used in part of the analysis. The surface heating/cooling is the sum of the turbulent sensible and latent heat fluxes and the net radiative heat flux, which is the combination of the net short wave and long wave radiative fluxes (Gill, 1982). Each of the radiative fluxes is the sum of the incoming and outgoing fluxes. In regions of partial ice cover, most atmospheric reanalyzes use an approach where each individual flux component is the weighted average of that over the open water and ice covered regions (e.g., Moore et al., 2015). This approach makes it challenging to retrieve open water fluxes in regions with fractional ice cover directly from the archived fields. For this reason, we used the following technique. The fields that characterize the surface meteorology, the 2-m air temperature and specific humidity, the sea-surface temperature, the 10-m winds, and the sea-level pressure, were obtained from the ERA5 reanalysis product. The COARE bulk flux algorithm was then used to estimate the open water sensible and latent heat fluxes from

the surface fields (Fairall et al., 2003). For the incoming long and short wave radiative fluxes, we assume that the ERA5 fields are representative of conditions over open water. For the outgoing long wave radiative flux, the assumption was made that the ocean surface emits as a blackbody with a temperature given by the sea surface temperature. The ERA5 ocean albedo (8.8%), along with the ERA5 incoming short wave radiative flux, were used to estimate the outgoing short wave radiative flux. The radiative fluxes estimated by this approach were shown to be in good agreement with the associated ERA5 fluxes over adjacent areas of open water.

2.4. One-Dimensional Mixing Model

To investigate aspects of the seasonal signal of hydrographic properties on the shelf, we use the one-dimensional mixing model of Price et al. (1986), hereafter referred to as the PWP model. It has been previously applied in a study of winter water formation on the Chukchi shelf by Pacini et al. (2019). The model uses the gradient Richardson number, the bulk Richardson number, and the vertical density gradient to assess when a hydrographic profile is gravitationally unstable, then initiates mixing until stability is restored. In this study, the model is forced by wind stress and buoyancy flux. The wind is taken from ERA5, and the heat flux is the open water flux described above. Freshwater forcing (evaporation minus precipitation and river discharge) is small in the region for the time of year that the model is run. According to ERA5, E-P is 0.2 mm/day, and according to Lammers et al. (2001) the effect of river runoff for the Chukchi Sea is order 1 mm/day, both of which had no appreciable effect on the model output. The impact of sea ice melt is investigated using the model. We used a time step of 3 h, and the initial hydrographic profile is discretized to 0.25 m in the vertical. At each time step, the observed heat flux and wind stress are applied to the profile and the model mixes the hydrographic properties until stability is achieved. Once the mixed layer is stable, the next time step is then evaluated. In this fashion, the model documents the temporal evolution of the mixed layer over the forcing period.

2.5. Historical Hydrographic Data

We use a climatological database of hydrographic profiles, described in Danielson et al. (2020). It is mainly comprised of the World Ocean Database 2018 from the National Centers for Environmental Information (Boyer et al., 2018). However, the climatology also includes a large number of hydrographic profiles measured by ships, profiling floats, and gliders provided by different national and international institutions. The additional data have been subject to a series of quality control measures described in Danielson et al. (2020). The time period of coverage is 1937–2019, although most of the data are from after 1980 and the majority of the profiles were obtained during the warm months of the year. Here, we consider the geographical domain encompassing the northeast Chukchi shelf.

3. Year-Long Mean Characteristics of Hydrography and Circulation

3.1. Mean Temperature, Salinity, and Velocity

We address first the year-long mean hydrography and velocity from September 1, 2013 to August 31, 2014 (realizing that some of the sites are missing some data within this 12-month span, Table 1; Figure 3). The annual mean near-bottom (i.e., at MicroCAT depth) potential temperature and salinity at each site are shown in Figures 4a and 4b (see also Table 2), and mean depth-averaged velocity vectors (over the ADCP range at each mooring) and associated standard error ellipses are shown in Figure 4c. The standard errors were estimated using the integral time scales for each of the moorings, based on the year-long timeseries. The integral time scale is taken to be the integral of the time-lagged autocorrelation function from zero lag to the first zero crossing (see Hogg et al., 1999). The degrees of freedom are defined as the record length divided by twice the integral time scale, which is used to compute the standard error (Hogg et al., 1999). In general, the mean temperatures are warmer in the south and colder in the north. The warmest values are found in Bering Strait, in particular at mooring A4 in the eastern part of the strait where the near-bottom temperature exceeds 9°C in September. This is because the mooring is located in the warm, fresh ACC (Woodgate, 2018). Progressing northward, the mean temperatures are warm along the coastal pathway and

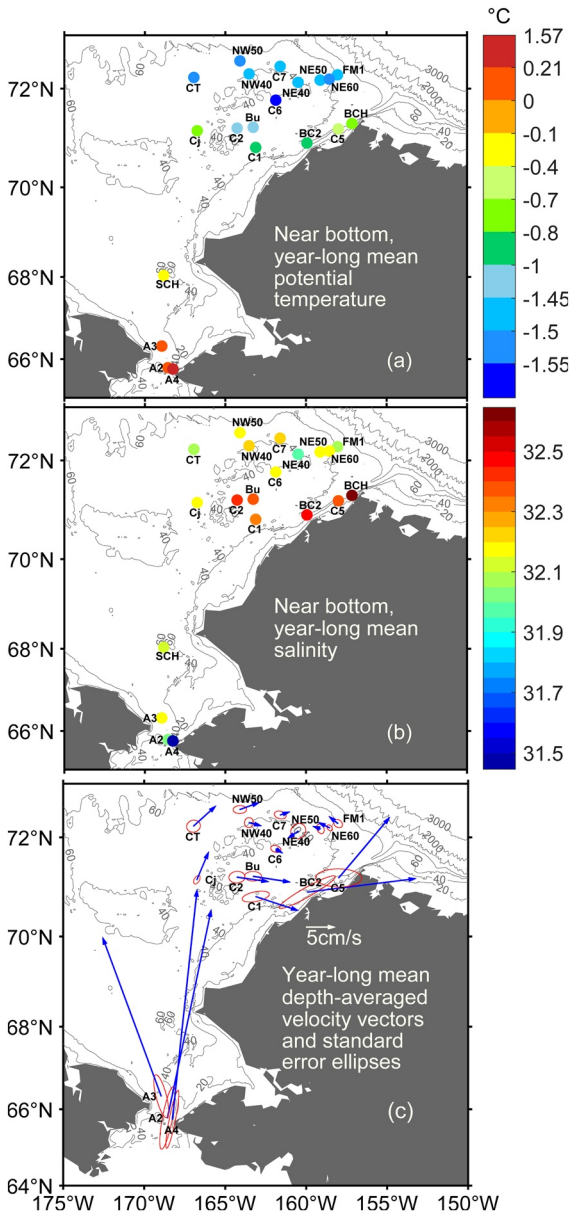

Figure 4. Year-long mean (a) potential temperature and (b) salinity at each site near the bottom. (c) Year-long mean, depth-averaged velocity vectors, and standard error ellipses at the mooring sites. The bathymetry is from IBCAO v3.

in Central Channel, reflecting the two branches of circulation in the eastern Chukchi Sea (Figure 1). In the vicinity of Hanna Shoal and the northern shelf, the mean temperatures are generally cold, in the range of −1° to −1.5°C, and display little geographical variation.

The pattern of mean salinity is different than that of temperature. The values in Bering Strait are the freshest, with a particularly low value at mooring A4 due to the influence of the ACC. Progressing northward, the mean values are higher, except that the moorings in or near the coastal pathway (C1, BC2, C5, and BCH), which were warmer than the central shelf, are saltier than the central shelf. This is opposite of what would be expected for the sites if salinity variation were due solely to the warm and fresh ACC. The explanation is that these locations were influenced by polynya/lead activity, which is known to occur adjacent to the coast on the northeast Chukchi shelf (e.g., Ladd et al., 2016).

To demonstrate this, we tabulated the number of days that the ice concentration dropped below 85% during 2013–2014, between freeze-up and melt-back (defined below), at each AMSR2 grid point on the shelf. These are referred to as polynya/lead days, and the distribution across the Chukchi shelf is shown in Figure 5. The vast majority of the time, this condition was met for at least two consecutive days at each of the mooring sites. We note that convection to the seafloor can occur within hours once the water starts to re-freeze in a polynya or small lead (Pacini et al., 2019). The increased periods of reduced ice cover along the coast seen in Figure 5, particularly in the region of Barrow Canyon, would thus lead to salinization of the water column and higher values of salinity at the above-noted moorings. One sees that moorings C2 and Bu, which are not in the coastal pathway nor in the region of polynya/lead activity, were also characterized by high values of salinity (Figure 4b). This is because the formation of polynyas and leads in the vicinity of Barrow Canyon is often associated with upwelling events in which the flow in the canyon is reversed (i.e., directed up-canyon; Pisareva et al., 2019). Our data reveal that these events also correspond to reversed flow (i.e., flow to the west) at moorings C2 and Bu (see Section 4.2). This implies that the salinized water from the polynya/lead region will advect under the ice to these two mooring sites, leading to the higher observed year-long mean salinities (note that this was not Atlantic Water). The effects of polynyas/leads are considered further in Section 4.1.3.

As was the case for the composite data set of Woodgate et al. (2005a), the depth-averaged, annual mean flow is strongest in Bering Strait. The largest value (~40 cm/s) was measured at mooring A4 in the ACC. The coastal pathway is characterized by strong flow as well, particularly in Barrow Canyon. The flow emerging from the Central Channel appears to bifurcate: some of it progressing to the latitude of Hanna Shoal and some of it heading east, presumably passing through gaps in the ridge that extends southwest of the shoal. This bifurcation has been noted before (Stabeno et al., 2018), and Pacini et al. (2019) present evidence of flow passing through one of the small gaps. On the northern shelf the mean circulation is weaker. As discussed in previous studies (e.g., Fang et al., 2020; Lin et al., 2019; Pickart et al., 2016; Weingartner, Fang, et al., 2017) the flow impinging on Hanna Shoal from the west circulates on both sides of the shoal. The anti-cyclonic northern pathway is evident in Figure 4c, which retroflects to the east on the south side of the shoal, joining the portion that circulated cyclonically south of the shoal to feed the Barrow Canyon inflow. The three moorings to the northeast of Hanna Shoal (NE50, NE60, and FM1) all show weak westward mean flow.

Table 2
Mooring Statistics

	Temperature (°C)		Salinity					
ID	Mean	Standard deviation	Mean	Standard deviation	Warm water appearance times	Cold water appearance times	Freeze-up dates	Melt-back dates
A2	0.20	1.99	32.00	0.56	05/06/2014	12/28/2013	12/19/2013	05/15/2014
A3	0.10	1.84	32.18	0.39	05/09/2014	12/31/2013	12/18/2013	05/16/2014
A4	1.57	3.45	31.45	0.98	05/04/2014	12/26/2013	12/17/2013	05/15/2014
BCH	−0.71	1.23	32.69	1.00	07/13/2014	12/02/2013	11/19/2013	07/18/2014
BC2	−0.86	1.24	32.50	0.75	07/14/2014	12/02/2013	11/20/2013	07/02/2014
Bu	−1.40	0.81	32.39	0.42	07/28/2014	12/04/2013	11/20/2013	07/04/2014
Cj	−0.77	1.41	32.19	0.33	06/26/2014	12/04/2013	11/24/2013	06/28/2014
C1	−0.86	1.30	32.34	0.45	07/13/2014	12/04/2013	11/22/2013	07/15/2014
C2	−1.32	0.92	32.41	0.38	07/16/2014	12/01/2013	11/20/2013	07/15/2014
C5	−0.44	1.43	32.36	0.86	07/12/2014	12/02/2013	11/19/2013	07/02/2014
C6	−1.55	0.29	32.19	0.34	08/24/2014	01/01/2014	10/31/2013	07/16/2014
C7	−1.48	0.32	32.20	0.40	08/09/2014	12/03/2013	10/25/2013	08/01/2014
CT1	−1.51	0.67	32.08	0.26	07/10/2014	12/04/2013	10/31/2013	07/03/2014
FM1	−1.47	0.24	32.09	0.37	09/08/2014	11/21/2013	11/11/2013	07/16/2014
NE40	−1.49	0.28	31.99	0.51	08/15/2014	01/08/2014	10/31/2013	07/16/2014
NE50	−1.50	0.22	32.18	0.38	08/24/2014	01/08/2014	10/31/2013	07/16/2014
NE60	−1.51	0.20	32.17	0.39	09/07/2014	01/20/2014	11/09/2013	07/16/2014
NW40	−1.49	0.47	32.23	0.31	08/29/2014	01/16/2014	10/26/2013	07/04/2014
NW50	−1.51	0.37	32.16	0.30	08/06/2014	11/30/2013	10/24/2013	07/30/2014
SCH	−0.11	1.55	32.13	0.44	05/16/2014	11/26/2013	12/18/2013	07/03/2014

Recently, Lin et al. (2019) compiled shipboard ADCP data from eight cruises that sampled the northeast Chukchi Sea during the months of May to October 2003–2017. They investigated the response of the circulation to different wind conditions, which revealed that the flow along the coast is sensitive to the wind stress, while the interior circulation varies according to the wind stress curl over the interior shelf. For all wind directions except northeasterly, the ACC advects water into Barrow Canyon. By contrast, strong northeasterly winds often drive up-canyon flow (i.e., it results in upwelling conditions; see also Pisareva et al., 2019; Weingartner, Potter, et al., 2017; Woodgate et al., 2005a). With regard to the interior circulation, negative wind stress curl favors anti-cyclonic circulation around Hanna Shoal, while positive wind stress curl leads to cyclonic flow around the shoal. Fang et al. (2020) performed an EOF analysis of their year-long mooring data and did not find a correlation between the dominant modes and the wind stress curl. They suggested that there could be seasonality to the importance of the wind stress curl in dictating the circulation north of Hanna Shoal.

According to the ERA5 data, in 2014 the period from May to October corresponded predominantly to non-upwelling conditions and negative wind stress curl in the interior. Using the shipboard ADCP data set compiled by Lin et al. (2019), we constructed a composite map of the depth-averaged flow on the northeast Chukchi shelf corresponding to those conditions, that is, considering only data points when the wind was not northeasterly in the coastal region and the wind stress curl was negative in the area near Hanna Shoal. The result is shown in Figure 6 in relation to the mean flow vectors from the moorings over the same seasonal period (where we have included contemporaneous data from additional moorings on the Chukchi and Beaufort continental slopes and the mouth of Barrow Canyon). The comparison between these independent data sets is quite remarkable. The strong ACC is evident, flowing into Barrow Canyon. The weaker flow stemming from the Central Channel veers to the east and divides around the two sides of Hanna Shoal prior to merging with the coastal pathway near the head of the canyon. The flow exiting the

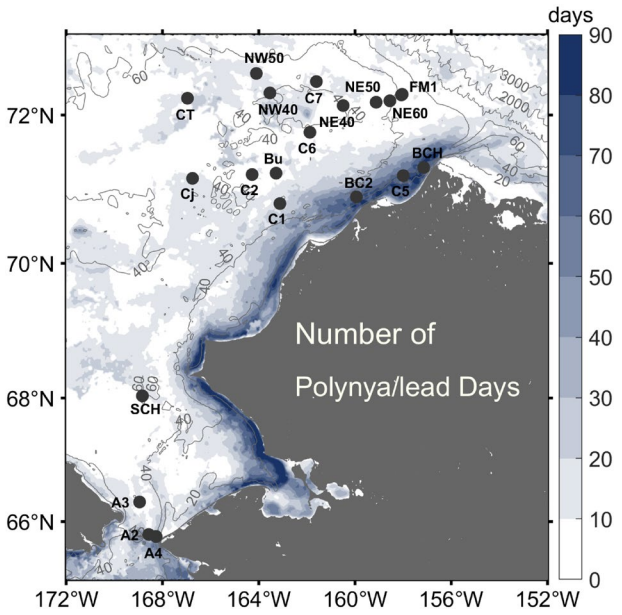

Figure 5. Number of days during the ice period (between freeze-up and melt-back) of 2013–2014 that the ice concentration fell below 85%, for each pixel of the Advanced Microwave Scanning Radiometer 2 product. The mooring locations are indicated by the black circles. The bathymetry is from IBCAO v3.

canyon then splits: some of it feeds the eastward-flowing Beaufort Shelfbreak Jet (Nikolopoulos et al., 2009; Lin et al., 2016; Pickart, 2004), and some of it turns westward to form the Chukchi Slope Current (Corlett & Pickart, 2017; Li et al., 2019; Stabeno et al., 2018).

3.2. Vertical Structure of Velocity

To address the vertical structure of the currents, we compared the year-long mean vectors averaged vertically over the surface layer (0–20 m) to those averaged vertically over the bottom layer (the bottom 20 m of the water column). Those sites in which the vertical coverage of the ADCP was less than 70% of the water column were excluded from the calculation (A3, C1, and C5). All of the vectors were significantly different than zero. This reveals that the strong flow through Bering Strait and along the coastal pathway into Barrow Canyon is in essentially the same direction from top to bottom (Figure 7), as per Roach et al. (1995) and Woodgate et al. (2015). The same is true of the moderately strong flow emerging from Central Channel, both to the north and to the east. By contrast, the circulation in the vicinity of Hanna Shoal, which is the weakest flow on the northeast Chukchi shelf, varies considerably in direction from the surface to the bottom. In general, the near-bottom flow follows the topography around the shoal more closely.

4. Seasonality

We now investigate the nature of the seasonal variations in temperature, salinity, and velocity across the eastern Chukchi shelf.

4.1. Hydrography

Using their year-long collection of moorings from 1990 to 1991, Woodgate et al. (2005a) noted that, broadly speaking, the deep part of the Chukchi shelf cools to the freezing point in late autumn and warms again in the spring/early summer. In terms of salinity, the deep shelf freshens in the fall (due to mixing of the cold, fresh surface water downwards), followed by salinization in the winter (due to ice formation) and freshening again in the spring/summer (likely due to downward mixing of surface freshwater). During the winter months, the water across the shelf "collapses" to a small range in temperature/salinity (*T/S*) space along (or close to) the freezing line. Fang et al. (2020) also described a rapid reduction in temperature in November/December in their moorings south of Hanna Shoal. Woodgate et al. (2005a) found that, particularly for salinity, the conditions on the shelf were largely dictated by input from Bering Strait, except in winter. We note again that our mooring coverage favors the northeast Chukchi shelf, whereas the moorings analyzed by Woodgate et al. (2005a) were spread out over the shelf with only two moorings in the northeast. It is thus unclear if the conclusions reached by them should apply to our mooring data. Furthermore, in any given year the atmospheric forcing, as well as Bering Strait input, could have notable differences.

4.1.1. Warm Water Appearance

To address the propagation of temperature and salinity across the shelf, we first focused on the spring transition from the cold winter *T/S* class to the appearance of warmer water at each site. To do this, we examined each temperature record and visually identified the start and end of the winter cold period. An example is shown in Figure 8a for mooring C1 northwest of Icy Cape. At some sites, there were brief periods where warmer water was present at the mooring in the middle of the otherwise cold period in winter. Such an event occurred from January 17 to 29 at mooring C1 (Figure 8a). At other sites, the warm water interruptions were more common. These fluctuations were not considered in the determination of the fall and spring transition times, and in each case the identification of the transition times was straightforward. Additionally, for each mooring we identified the time of freeze-up and melt-back using the ice concentra-

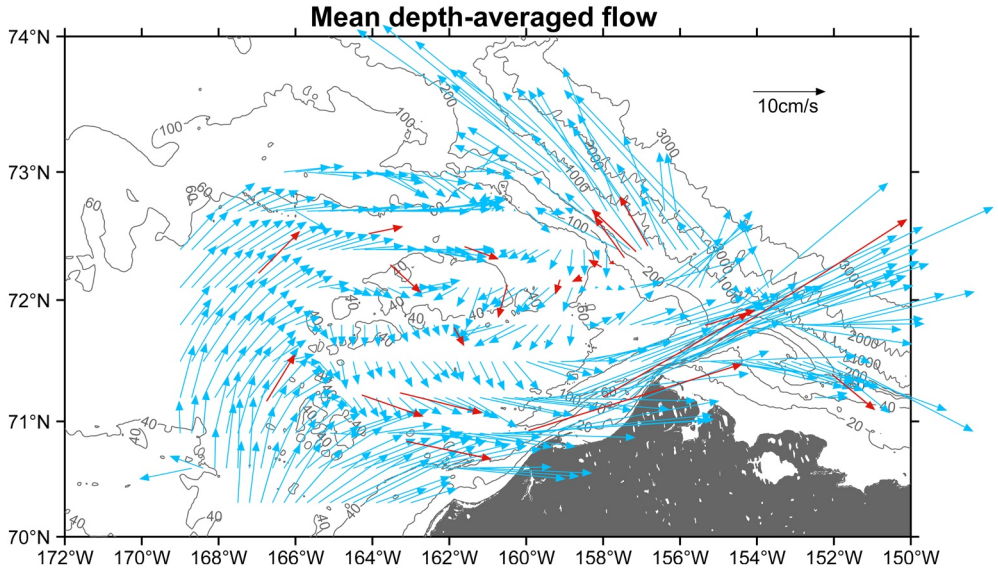

Figure 6. Comparison of depth-averaged shipboard ADCP currents (cyan vectors) to the depth-averaged moored ADCP currents (red vectors). Both sets of measurements are averaged over the time period May–October, where the shipboard map only includes non-upwelling/negative interior wind stress curl time periods; see text for details. The five moorings over the Chukchi slope, two moorings near the mouth of Barrow Canyon, and an eastern mooring at the Beaufort shelfbreak are analyzed elsewhere. The bathymetry is from IBCAO v3.

tion data in the vicinity of the site. Freeze-up was defined as the date when the ice concentration first exceeded 90%, while melt-back was taken to be when the ice concentration last fell below 90%. This is shown for mooring C1 in Figure 8b.

The warm water appearance times so identified are shown in Figure 9a. In the figure, we list the appearance date at each site, and use color to denote the number of elapsed days since the appearance of warm water in Bering Strait. The summer water first appears in the strait in early May. Roughly 2 months later, the Central Channel site warms (late-June), and 2 weeks after that the warm water appears at the mooring north of Central Channel. About the same time, the four moorings along the coastal pathway record the appearance of warm water. Thus, the water feeding Barrow Canyon warms roughly two and a half months later than that entering Bering Strait. The latest appearance dates are found in the vicinity of Hanna Shoal, with the two sites to the northeast of the shoal not warming until early September, roughly 4 months later than in Bering Strait.

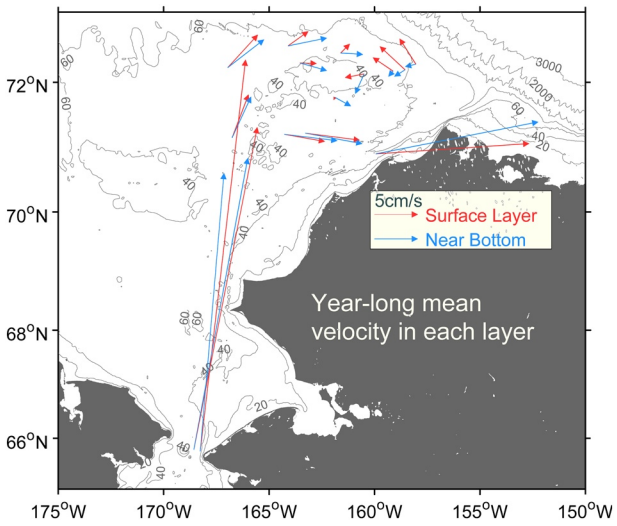

Figure 7. Year-long mean velocities in the surface layer (red) and in the near-bottom layer (blue) for each of the moorings. The bathymetry is from IBCAO v3.

Is this space-time pattern consistent with advection? This would seem to be the most plausible explanation since the instruments are near the bottom and hence less apt to be impacted by solar heating. To answer this, we assume a near-bottom circulation pattern dictated by Figure 7 (where the blue vectors correspond to the bottom layer). In particular: (a) the water in the coastal pathway feeds Barrow Canyon; (b) the water emanating from Central Channel bifurcates, with some of it flowing northward to the latitude of Hanna Shoal and some of it veering eastward towards the coast; and (c) the water reaching the northwest part of Hanna shoal circulates anticyclonically around the shoal to its southern side. These flow patterns are further justified below. We have not considered the water that reaches Hanna Shoal from the western pathway (see Figure 1) because we have no data from that pathway. However, because of the much longer length of that pathway, any warm water reaching Hanna Shoal via that route will clearly arrive much later than via the Central Channel route.

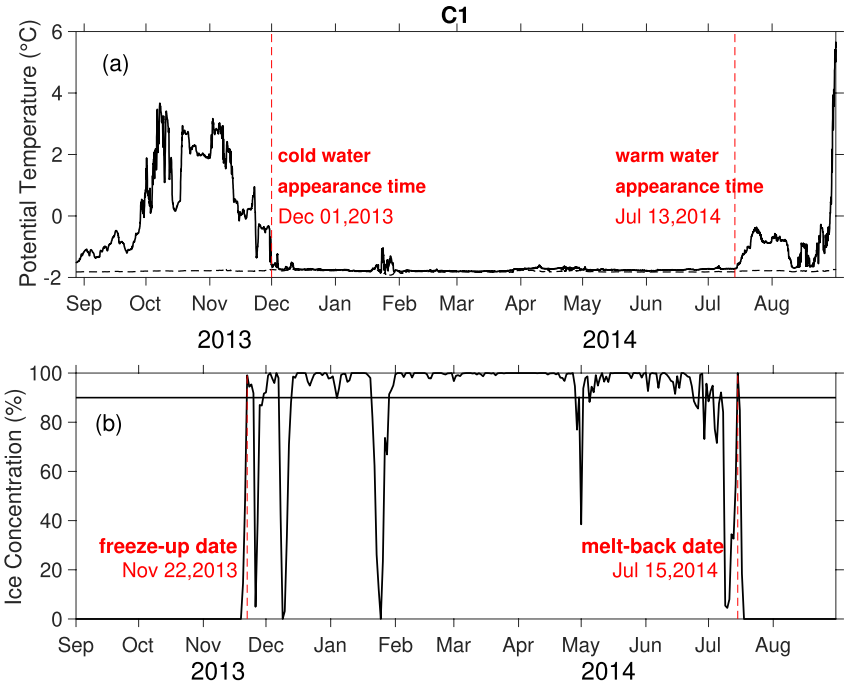

Figure 8. (a) Temperature timeseries at mooring C1 (the MicroCAT is situated at 40 m), northwest of Icy Cape. The cold water and warm water appearance times are marked. The black dashed line is the freezing point temperature. (b) Ice concentration timeseries at mooring C1, where the freeze-up and melt-back dates are marked. The solid black line denotes 90% concentration, used to define freeze-up and melt-back.

To track the warm water as it progresses between two given moorings, we computed the average near-bottom velocity over the time period between the appearance of the warm water at the first site and that at the second site. The mean of these two values was then used to compute an advective time for each mooring

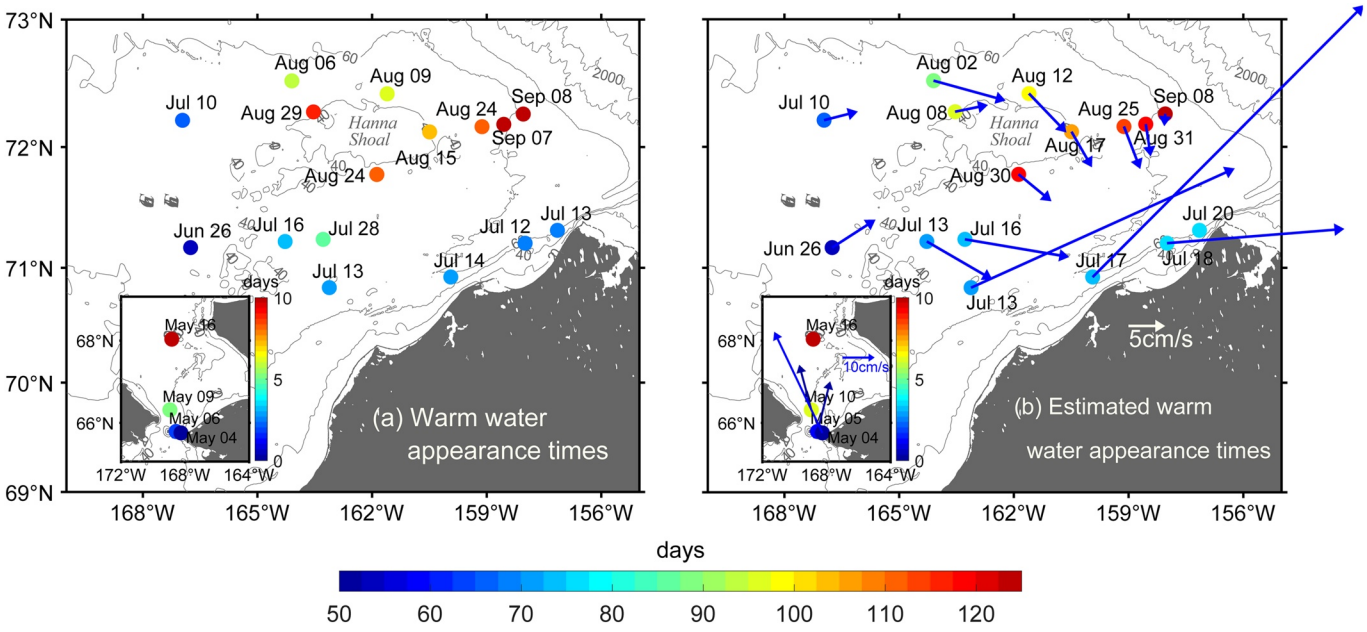

Figure 9. (a) Warm water appearance times at each of the moorings, where the inset shows the region of the southern moorings. The color denotes the elapsed time in days from the appearance of warm water in Bering Strait (day 0 at mooring A4). Note the different color bars for the two different regions. (b) Predicted warm water appearance times based on advection (see text for details). The blue vectors denote the mean near-bottom flow at each mooring as the warm water progressed from that site to the next site. The bathymetry is from IBCAO v3.

pair (in the two cases where there was no velocity at the downstream mooring, we used the upstream time average). The progression of moorings considered in the calculation is indicated in Figure 10; note that in some cases a single upstream mooring is paired with more than one downstream mooring, which is a necessity due to our mooring coverage. The extreme case of this is the Central Channel mooring (Cj) which connects with the mooring to the north as well as the one to the east. This is reasonable because it is known that the flow emerging from the channel bifurcates as such (Figure 6; see also Pacini et al., 2019). Because of the large distance between the Bering Strait moorings and those on the northeast shelf, we did a separate calculation for the two regions (recall that there are no velocity data at mooring SCH near Point Hope; Figure 1). In the northern region, the starting mooring for the coastal pathway is C1, and the starting mooring for the two central shelf pathways is mooring Cj. In the southern region the starting mooring is A2 (see Figure 10).

Using the above-determined advective times for each mooring pair, we calculated the predicted warm water appearance time for each successive mooring along the four pathways in Figure 10. The predicted times are shown in Figure 9b, presented in the same fashion as the actual appearance times in Figure 9a. Note that the three starting moorings (A2, Cj, and C1) have the same appearance date in both panels, by definition. It is worth noting that, using these three appearance dates plus the distances between mooring A2 and the two northern sites, Cj and C1, this implies an advective speed of approximately 12 cm/s, which is in line with the estimate in Pickart et al. (2016) for this same region. In Figure 9b, we show the mean near-bottom flow vectors at each mooring over the time period that warm water progressed from that mooring to the next.

Overall, there is good agreement between the observed and predicted warm water appearance times (compare Figures 9a and 9b). The advective calculation successfully predicts that the water emanating from Bering Strait reaches the latitude of Pt. Hope in roughly 10 days, while it takes over a month for the water veering to the east from Central Channel to progress across the corrugated topographic ridge. The strong velocities in the coastal pathway imply that it takes a week for the warm water to advect from the Icy Cape region to Pt. Barrow (Figure 9b), whereas the actual warm water appearance times indicate that the warm water essentially appears simultaneously at these four sites (Figure 9a). The salient point is that the progression is very rapid in this part of the domain. The observed progression of warm water from Central Channel northwards, then anticyclonically around Hanna Shoal, is also well explained by advection. This includes the very late appearance dates at the three moorings to the northeast of the shoal (NE50, NE60, and FM1).

Numerous previous studies, both modeling and observational, have estimated residence times for water traversing the Chukchi shelf. Generally speaking, the estimates depend on the pathway in question, the time of year, and the wind forcing. Using a barotropic model, Winsor and Chapman (2004) investigated the sensitivity of the residence time to wind. They calculated a travel time of less than 6 months from Bering Strait to Barrow Canyon for all wind directions except easterly. The transit time lengthened considerably for winds out of the east. Spall (2007) invoked a travel time tracer in a primitive equation model of the Chukchi shelf and found that the water in Barrow Canyon generally took 6–8 months to arrive there from Bering Strait. This represents a mix of waters that took the fairly direct route along the coast, and waters that circulated via the longer, slower route through Herald Canyon and Central Channel before turning eastward to join the coastal route. Consistent with this, Shroyer and Pickart (2019) used an idealized model to isolate the coastal and interior pathways, and found transit times of 6 months or more.

Different observational approaches have been applied to estimate the transit times. Similar to the calculation done here, Weingartner et al. (1998) used the arrival time of the 0°C isotherm from Bering Strait to Barrow Canyon to deduce a mean advective speed of 10 cm/s and a time of 2.5 months. Stabeno (2018) calculated the coastal transit time to be a bit over 3 months using surface drifters. Using their set of moorings, Woodgate et al. (2005a) estimated the time to be from several to six months, depending on the time of year. Overall, the previously determined travel time estimates for water to progress from Bering Strait to Barrow Canyon range from a few months to a half-year or more, depending on the different factors mentioned above.

Our results can be used to estimate the range in warm water transit times from Bering Strait to Barrow Canyon for the year of our study (spring/summer 2014). The fastest progression occurred along the coastal pathway, which was 2.5 months. This is the same value determined by Weingartner et al. (1998) and similar to the drifter-derived value of Stabeno et al. (2018). In Figure 9, it is seen that the warm water arrived at

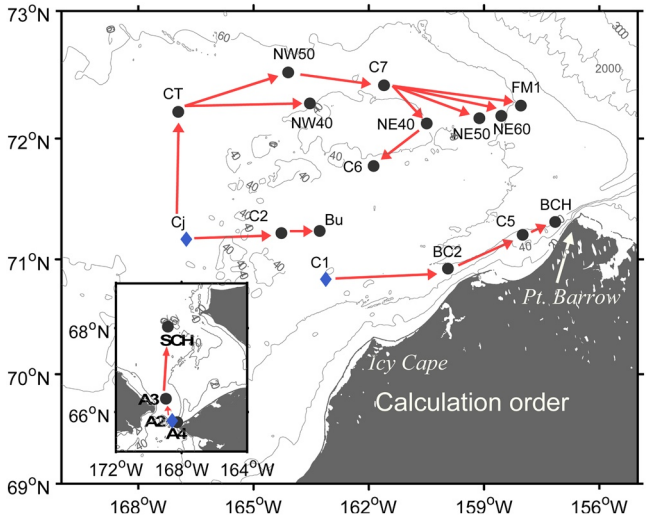

Figure 10. Schematic showing the chosen progression for the advective calculation of warm water appearance times (the red vectors do not represent data). Moorings A2, Cj, and C1 (blue diamonds) are the starting moorings for the three calculations. The bathymetry is from IBCAO v3.

the northeastern part of Hanna Shoal in late-August/early September via the slower Central Channel pathway. According to the shipboard ADCP circulation map in Figure 6, from there the water continues around to the south side of Hanna Shoal and then retroflects cyclonically into Barrow Canyon (see also Fang et al., 2020). Integrating the shipboard ADCP data from Figure 6, we compute a travel time of approximately 2 months for the water to travel from the northeast part of the shoal to mooring BCH in Barrow Canyon. Therefore, the range in time for warm water to travel from Bering Strait to Barrow Canyon is 2.5–6 months, via the fastest and slowest pathways, respectively. It should be remembered that the winds during this period were generally not conducive for upwelling, which favors shorter residence times.

4.1.2. Cold Water Appearance

The cold water appearance times are shown in Figure 11a (where we have color coded the appearance dates relative to mooring CT in the northwest part of the domain, where the cold water appeared first). It is immediately clear that, unlike the progression of warm water, advection is not playing the primary role in dictating the appearance of the cold water across the shelf. For instance, the cold water appears along the coastal pathway feeding Barrow Canyon before appearing in Bering Strait. As such, it makes no sense to try an analogous advective calculation as was done for the warm water. It is likely that enhanced air-sea heat loss in the fall, together with stronger wind mixing and the presence of ice, influence the appearance of the cold water. As described in Weingartner et al. (1998), densification of the surface water in winter due to ice formation and brine rejection results in convective overturning that brings the cold, salty water to depth. The shallow depth of the Chukchi shelf means that the overturning can reach the bottom fairly quickly (Pacini et al., 2019). This is especially true since the water column stratification is already reduced due to enhanced wind mixing during the fall storm season (Ardyna et al., 2014).

To shed light on this, we plotted the time of freeze-up at each mooring site (Figure 11b, where the color coding denotes the date relative to mooring NW50 in the northwest part of the domain, where freeze-up occurred first). Recall that freeze-up is defined as when the ice concentration first exceeds 90% (see Figure 8). As expected, the Chukchi shelf generally froze from north to south, taking roughly seven weeks (late-October to mid-December). Comparing Figures 11a and 11b, it is apparent that there is not a one-to-one correspondence between freeze-up at a site and the appearance of cold water near the bottom at the mooring. This motivated us to consider the different factors noted above, heat flux, wind, and ice, more closely.

4.1.2.1. Central Shelf

On the central part of the shelf in the vicinity of 71°N, freeze-up occurred in late-November at all seven moorings, and roughly 10 days later cold (near freezing-point) water was recorded at all seven sites (Figure 11c). While there are differences from mooring to mooring, the general pattern at these locations was an overall cooling/freshening of the bottom water during the preceding month, with an interruption to warmer and saltier conditions shortly before the onset of the cold-water period (Figures 12a and 12b). This indicates that the appearance of cold water near the freezing point (around December 2) is not associated with brine rejection and associated gravitational overturning, otherwise the cold signal would coincide with salinification. It is also not due to advection from Bering Strait, since, as noted above, cold water does not appear at the southern moorings until later. We believe that wind-driven vertical mixing leads to this signal. This is consistent with Woodgate et al. (2005a) who argued that wind mixing led to the autumn freshening measured in their bottom moorings.

To investigate the appearance of the cold and fresh water at bottom, we invoked the one-dimensional PWP model. For an initial profile, we averaged all the November stations in the historical climatology in the vicinity of 71°N (there were only 35 such profiles). For the forcing, we used the ERA5 wind and the open

water heat flux data for November–December 2013, as described in Sections 2.2 and 2.3. These are shown in Figures 13c and 13d, which reveal that there were numerous synoptic events over the course of the month leading up to the appearance of cold water. The model computes the surface stress as the difference between the induced velocity of the water column and the strength and direction of the winds, which is used to impart momentum to the profile.

The simulation was carried out from October 25 to December 5, 2013. The reader should keep in mind that the initial hydrographic profile was not contemporaneous with the time period, although the near-bottom temperature and salinity are generally consistent with the mooring data prior to the appearance of the cold water. During this 6-week time period, the near-bottom circulation was similar to the mean pattern in Figure 4c. While in theory advection could be important, not only is there is no source of cold, fresh water from the south, advection could not explain the near-simultaneous appearance of the water at all seven moorings.

We first seek to understand whether the observed forcing is able to overturn the water column, and, if so, what controls the one-dimensional dynamics of the system. In order to test the sensitivity of the profile to overturning, a number of cases were run, the results of which are detailed in Table 3. In the first run, using the observed wind and heat flux, the profile overturned to the bottom early in the simulation (blue curves in Figures 13a and 13b). In order to assess the impact of synoptic storm events, when the windspeed is on the order of 10 m/s for 1–2 days, the timeseries of wind was lowpassed with a second-order 5-day Butterworth filter (Figure 13c). In this case, the profile did not overturn, even by the end of the simulation (green curves in Figures 13a and 13b). Not surprisingly, the same was true when the heat flux timeseries was similarly low-passed. However, using the synoptic winds and low-passed heat flux, the profile again overturned. This highlights the importance of the synoptic wind events for homogenizing the water column due to wind mixing. It should be noted that even when the heat flux is greatly reduced (total heat flux of 100 W/m^2) the profile still overturns due to the synoptic winds. However, the final temperature of the profile in that case is much warmer than the freezing point.

While these sensitivity simulations are consistent with the overall cooling during the weeks leading up to the appearance of cold-water, they cannot explain the concomitant freshening. This is because, once the overturning reaches the bottom, the salinity undergoes no further decrease. What might be the cause of the continued freshening? We suspect that intermittent melting of the newly formed ice could be the reason, in the same way that the advancing ice edge deposits fresh water on the Bering Sea shelf (Zhang et al., 2010). The satellite ice concentration data indicate that the ice edge was loitering as it encroached on this set of moorings (this can be seen in late-October/early November at the Bu site in Figure 12c). Also, most of the wind events until mid-November were associated with southerly winds (Figure 13c), bringing warmer air from the south. The idea is that fresh water from the melting ice was getting continually introduced to the region, then subsequently mixed into the water column during the synoptic events.

To test this hypothesis, we did a set of PWP simulations where fresh water was added in pulses during the run to mimic the loitering. Here, we describe one particular run, although numerous variations of this simulation led to the same general temperature and salinity evolution. While using the synoptic forcing timeseries as described above, fresh water was introduced to the top grid point of the water column every two days from November 3 to 13, 2013, coincident with the loitering ice edge over the range of mooring locations. This corresponds to a cumulative addition of 1.5 m of freshwater to the water column, comparable to the amount of freshwater present at the surface near the ice edge in observations on the Chukchi shelf (Lu et al., 2020). Over the first two weeks of November, such forcing produces gradual cooling and freshening near the bottom of the profile through overturning of the water column due to the synoptic storm events.

Around November 18, the mixed layer reaches the freezing point, which means that ice could start to form. In reality, a warm, salty anomaly appeared at this latitude shortly after that (Figures 12a and 12b), likely advected from the north due to the northerly winds that began around November 16 (Figure 13c). Obviously, the one-dimensional PWP model cannot capture this scenario. Hence, we temporarily turned off the heat flux forcing when the freezing point was reached, until the wind was able to mix the cold water with the warmer water beneath the mixed layer, leading to a warmer mixed layer. At the end of November, a strong southerly wind event with enhanced heat flux occurred. In the observations, this synoptic event coincided

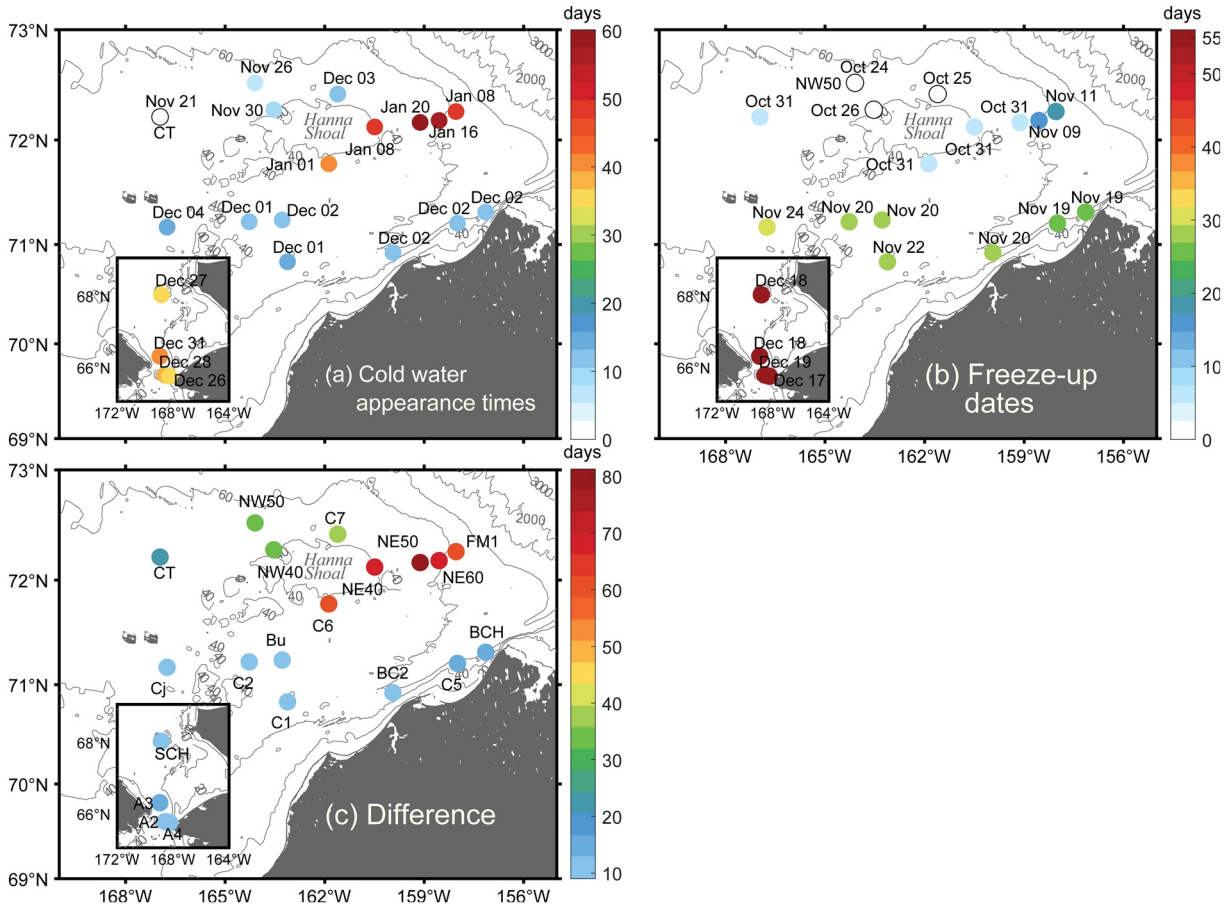

Figure 11. (a) Cold water appearance dates identified using the mooring timeseries. The inset in the lower left shows the southern moorings. The color denotes the day of appearance relative to mooring CT. (b) The freeze-up date at each mooring computed using the ice concentration data. The color indicates the offset in days from freeze-up at mooring NW50. (c) The elapsed time between freeze-up and the appearance of cold water. The bathymetry is from IBCAO v3.

with the disappearance of the warm, salty anomaly and the onset of the cold period (Figures 12a and 12b). This was simulated with the inclusion of one final freshening event in the PWP model on November 28. The strong synoptic winds mixed this freshwater pulse away and the synoptic heat flux reduced the temperature of the profile to the freezing point. By the end of the simulation (December 5), the depth of the mixed-layer was only a few meters from the depth of the sensor (located 5 m above the bottom).

Our PWP simulations have thus identified a plausible mechanism by which the near-bottom water cools to the freezing point, marking the beginning of the extended cold period, while at the same time the near-bottom salinity decreases. The simulated change in salinity is less than that observed at the Bu mooring (0.3 vs. 0.7), but it should be remembered that the initial profile used here was not from 2013, and there are other factors, such as advective anomalies, that cannot be accounted for. Interestingly, the salinity began to increase at mooring Bu after the cold water arrived (Figure 12b), consistent with brine-driven convection due to ice formation over the site.

4.1.2.2. Northeast Shelf

In contrast to the set of moorings near 71°N, the cold water appeared roughly 1–1.5 months later at the five moorings extending from south of Hanna Shoal to the northeast (Figure 11a). The relative timing of this appearance since freeze-up was 2–2.5 months, compared to order 10 days near 71°N (Figure 11c). Why didn't wind-driven convection, in conjunction with air-sea heat loss, lead to a similarly rapid appearance of cold water as for the southern sites? Both the heat flux and wind forcing were similar in the two regions (not shown). We argue that enhanced stratification of the water column at the five sites south and east of Hanna

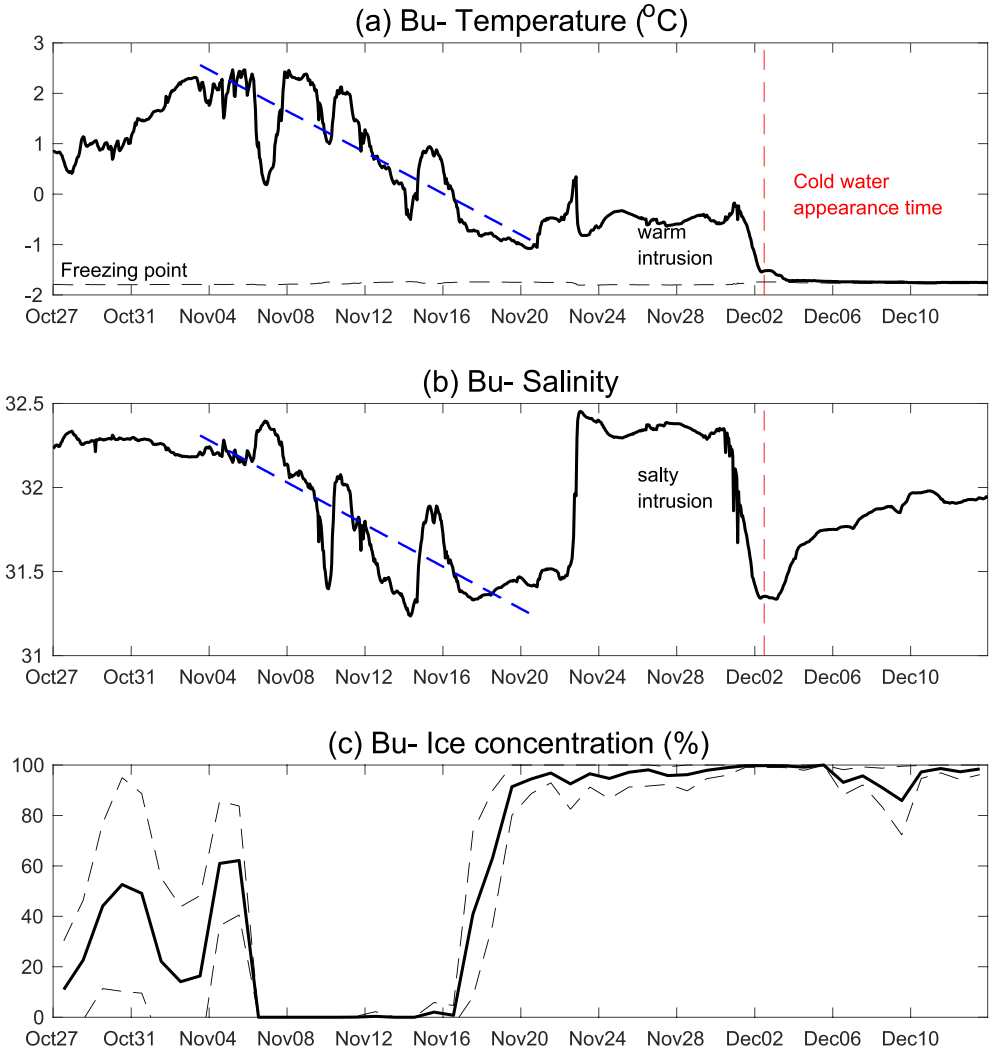

Figure 12. (a) Temperature at mooring Bu, which is one of the sites near 71°N, and (b) salinity at mooring Bu. The black dashed line in (a) is the freezing point temperature. The red dashed line marks the cold water appearance time. The blue dashed line is the linear regression for temperature and salinity from November 4 to 20, 2013, indicating the overall cooling and freshening at the site prior to the appearance of the warm, salty intrusion (which is marked). (c) Ice concentration, averaged in a 0.5° × 0.5° box around mooring Bu, where the dashed lines denote the standard deviation.

Shoal prohibited such wind-driven overturning, and the cold water more likely propagated from upstream (i.e., from the south).

Using the historical hydrographic data set described in Section 2.5, we computed the vertical profile of buoyancy frequency for each cast, $N = \sqrt{-\frac{g}{\rho_0}\frac{\partial \rho}{\partial z}}$, where ρ is the depth-dependent potential density, g is the gravitational acceleration, and ρ_o is the mean density. We then tabulated the maximum value of N for each profile. Figure 14a shows the lateral distribution of the maximum N, grided using the profiles over the months of September and October as an indication of the stratification of the water column prior to the onset of freeze-up (we excluded the small number of casts in November which caused biases). The map was made by interpolating the data onto a 0.05° by 0.05° grid using an interpolation scheme that gives preferential weighting along the isobaths (see Våge et al., 2013). The distribution reveals that the pycnocline is stronger in a band surrounding the eastern and southern sides of Hanna Shoal, which encompasses the locations where the cold-water appearance times were much later (indicated by the stars in Figure 14a). By contrast, the moorings along 71°N, where the cold water was measured early in the season near freeze-up,

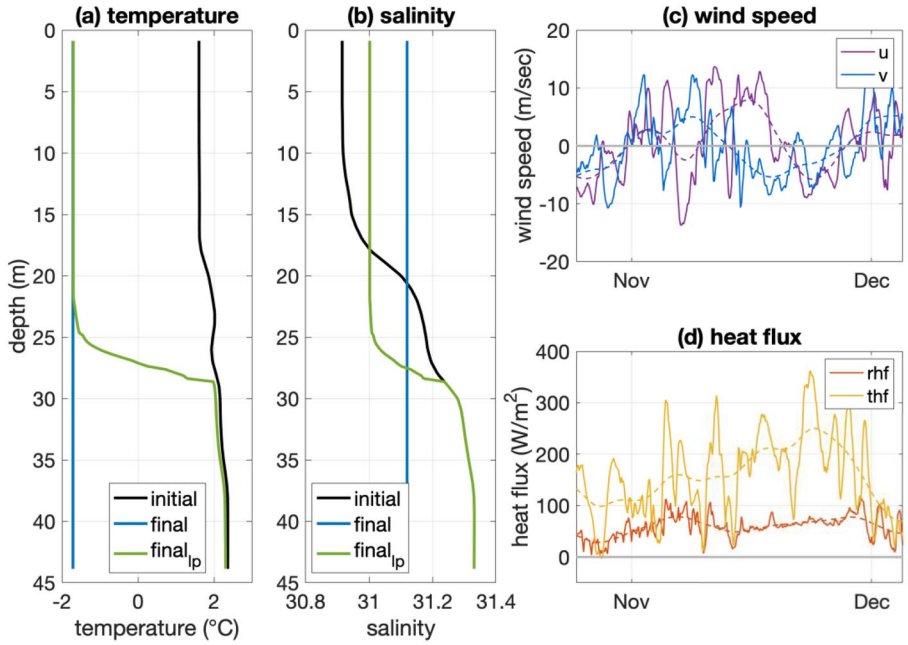

Figure 13. (a) Initial temperature profile and final temperature profiles, where the lp subscript denotes the case with low-passed wind forcing, for the two PWP simulations in bold in Table 3. (b) Same as (a) except for salinity. (c) Zonal and meridional wind speed (u and v) over the forcing period, averaged over the region 70°–71.5°N and 168°–160°W. The solid line is the 3-hourly data and the dashed line is the 5-day lowpassed timeseries. (d) Same as (c) except for total turbulent (yellow) and net radiative (orange) heat flux. Positive flux means heat loss from the ocean to the atmosphere.

are in a region corresponding to a weaker pycnocline (squares in Figure 14a). This pattern is consistent with synoptic measurements as well (Fang et al., 2017; Weingartner, Fang, et al., 2017).

The reason why the stratification is stronger on the eastern/southern side of Hanna Shoal is the presence of a surface layer of freshwater. This is seen in Figure 14b which shows the average salinity in the upper 10 m of the water column. Again, the moorings with delayed cold water appearance times stand out. Note also that the surface temperature is cold in this region (Figure 14c). We suspect that this pool of cold, fresh, highly stratified water is due to the timing of the seasonal melt-back. To elucidate this, we used the AMSR2 ice concentration data from 2012 to 2019 to compute a climatological map of melt-back time (Figure 14d). One sees that the pack ice melts later on the north side of Hanna Shoal. This typically takes place in early July, which will result in cold, fresh melt water at the surface. Over the next few months, as the water progresses anti-cyclonically around Hanna Shoal (Figure 6), wind mixing should deepen the fresh water signal, resulting in the patterns documented in Figures 14a–14c.

As a final step to determine if the enhanced stratification around the southern/eastern side of Hanna Shoal could prohibit wind mixing to reach the bottom in the fall, we ran the PWP model with the same synoptic wind and heat flux forcing as above, except we used the average hydrographic profile computed from all the November casts in the northern region (26 profiles total). In this case, the water column did not wind mix

Table 3
PWP Experiments, With Outcome of Overturning to the Bottom

	2013 wind	2013 wind without synoptic events ($wind_{lp}$)	2013 wind with northern hydrographic profile
2013 heat flux	**Yes, 17 days (November 11)**	**No**	No
2013 heat flux without synoptic events ($heat_{lp}$)	Yes, 17 days (November 11)	No	No

The simulations are performed from October 25 to December 5, 2013. The bolded simulations are shown as examples in Figure 13. If a profile overturned, the time it took to do so is listed.

to the bottom due to the stronger surface stratification (Table 3). Instead, the slowly deepening mixed layer quickly cooled to the freezing point, which would lead to ice formation. The same thing happened when using the low-passed heat flux timeseries (as well as using both the low-passed wind and low-passed heat flux timeseries). This indicates that, even without synoptic storms, the background surface cooling leads immediately to ice formation since the cold water cannot get mixed through the strong pycnocline. As an extreme case, we turned off the heat flux altogether, which allowed the wind mixing to continue for the entire month. Still the water column did not overturn to the bottom, plus the temperature of the mixed layer was far warmer than the freezing point. These results imply that the appearance of the cold water to the east and south of Hanna Shoal was likely due to advection of the water from the south via the Central Channel pathway, where it was transformed via wind-driven overturning before flowing under the pack ice. This is consistent with the results of Fang et al. (2020).

4.1.3. Salinity Signals

As shown above, while the timing of the warm water appearance across the Chukchi shelf in spring/summer can be explained by advection from Bering Strait, this is not the case for the appearance of the cold water in the fall/winter due to other factors. It is similarly difficult to discern an advective pattern associated with the variation in salinity across the shelf. This is likely related to the formation of ice. When a polynya or lead forms in winter, the re-freezing of the water rejects brine that can destabilize the water column and quickly lead to convection reaching the seafloor (Pacini et al., 2019). This will lead to an increase in salinity measured by a bottom mooring. This process is well-documented in previous studies (e.g., Weingartner et al., 1998). Woodgate et al. (2005a) noted that the polynya/lead activity on the Chukchi shelf during the winter of 1990–1991 was lower than normal, which is why they were able to detect evidence of advection. We constructed a map of polynya/lead activity for 1990–1991, analogous to what was done above for our study year. This revealed that polynyas and leads during our study period were present in the coastal region roughly 3 weeks more than the earlier period.

These results make it unsurprising that we were not able to detect advective patterns among the salinity timeseries in our collection of moorings. To shed further light on this, we used the AMSR2 ice concentration data to tabulate the occurrences of openings in the ice at each of the mooring locations (see Figure 5). As was done earlier, we documented the number of days that the concentration fell below 85% during the period of winter ice cover (freeze-up to melt-back). Results are not sensitive to this exact choice. This information was then regressed against three different metrics that might be reflective of local salinization due to polynya/lead activity: the average salinity during the period of ice cover; the average value plus one standard deviation; and the maximum value recorded during this period. These regressions are shown in Figure 15, which show statistically significant relationships in all three cases (confidence level > 95%). We note that the three Barrow Canyon moorings have the highest salinities and the largest number of polynya/lead days. This is not surprising because of the common occurrence of the Northeast Chukchi polynya (Hirano et al., 2016; Ladd et al., 2016). Hence, unlike the situation in 1990–1991 presented in Woodgate et al. (2005a), we find that the polynya/lead activity during 2013–2014 was significant enough to be reflected in the salinity timeseries. It is worth noting that Woodgate et al. (2005a) had no moorings in the vicinity of the Northeast Chukchi polynya.

4.2. Velocity

We now compare conditions on the shelf when the seasonal mean flow is strong versus weak. We contrast two four-month periods during the year, referred to as the fast and slow periods. These were determined by computing the monthly mean speed at each site in the direction of the predominant (year-long average) flow at each location. This revealed that the weakest flow across the shelf occurred during the period December–March (mean velocity of 3.2 ± 3.0 cm/s) and the strongest flow occurred from May to August (mean velocity of 14.6 ± 1.8 cm/s; the uncertainties denote standard error). The biggest differences were in Bering Strait and the sites along the coastal pathway. This is consistent with the 1990–1991 climatology of Woodgate et al. (2005a).

The depth-averaged flow vectors during the fast period are shown in Figure 16a. The circulation pattern is generally the same as it is for the year-long mean, except the magnitude of the flow is considerably stronger

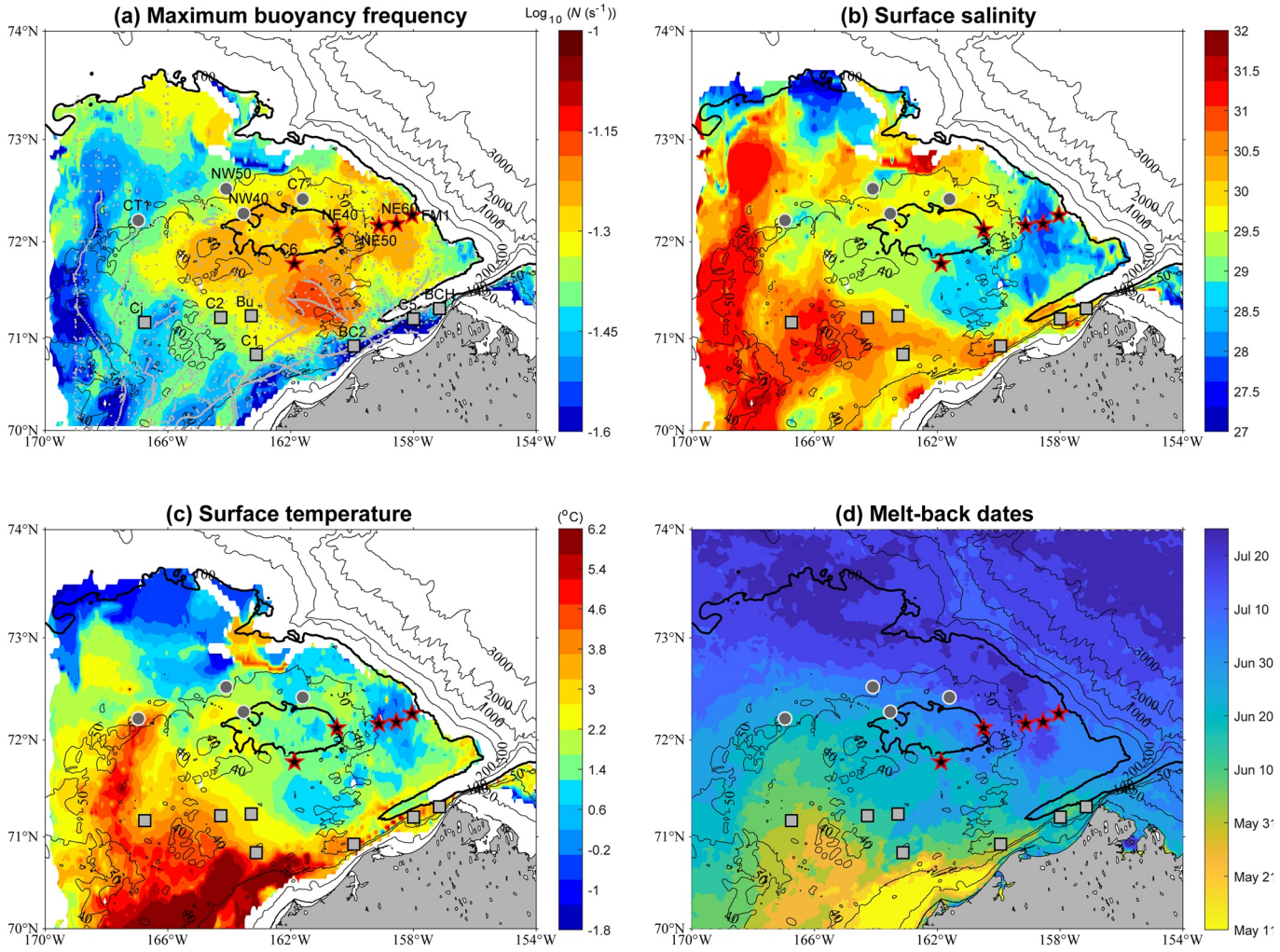

Figure 14. (a) Gridded map of the maximum value of buoyancy frequency in the water column in September/October (color) on the northeast Chukchi shelf, calculated using the hydrographic profiles from the climatological database. The small gray dots indicate the data points. The coverage is limited to bottom depths shallower than the 100 m isobath (indicated by the thick black line). The stars denote the moorings where cold water was not measured until late in the season, well after the onset of ice at the site. The squares denote the moorings where the cold-water appearance times occurred 1–1.5 months earlier, near the time of freeze-up. (b) Same as (a) except for salinity averaged over the top 10 m. (c) Same as (b) except for potential temperature. (d) Average date of melt-back during the period 2012–2019, calculated using the AMSR2 ice concentration data. The bathymetry is from IBCAO v3.

(compare Figures 16a and 4c). In Bering Strait, the magnitude of the velocity is 57.7 ± 2.5 cm/s at mooring A4, versus 49.9 ± 2.9 cm/s when averaged over the year. As demonstrated in previous studies (e.g., Woodgate, 2018), this mooring measures the ACC during the summer months, which is a seasonal strong, surface-intensified current transporting warm Alaskan Coastal Water generally northward. The flow along the entire coastal pathway is enhanced in Figure 16a for this reason. In the interior, the flow is also stronger relative to the mean, with generally anti-cyclonic flow around the north and east sides of Hanna Shoal.

As noted above, Lin et al. (2019) investigated the response of the circulation on the northeast Chukchi shelf to different wind forcing, using their extensive shipboard ADCP data set. They found that, while the coastal flow was sensitive to the wind stress, the circulation in the interior shelf was predominantly influenced by the wind stress curl. In particular, when winds near the coast were out of the northeast and exceeded 5.5 m s^{-1}, the coastal flow was reversed (i.e., towards Bering Strait), while for all other wind directions the coastal current was directed to the northeast and enhanced relative to the mean. For the interior, under conditions of negative wind stress curl the flow was generally directed anti-cyclonically around the north and east sides of Hanna Shoal, and for positive wind stress curl the opposite was true. The reason for this is

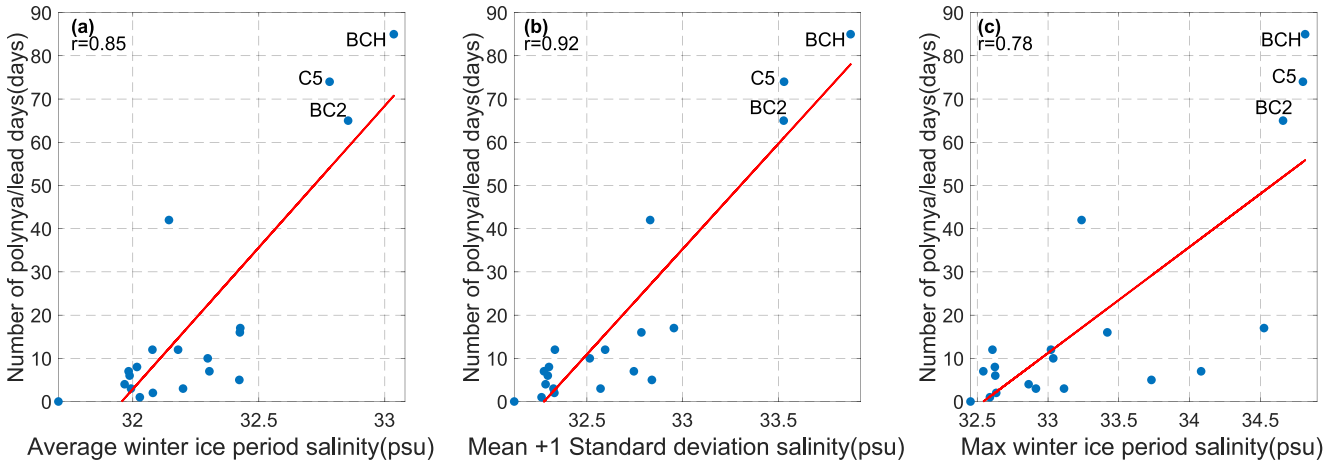

Figure 15. Number of polynya/lead days (ice concentration threshold is 85%, see text) at each site versus (a) mean salinity, (b) mean salinity plus one standard deviation, (c) maximum salinity measured by the mooring during the period of winter ice cover. The red line is the linear fit (confidence level > 95%).

the increase (decrease) in sea surface height on the shelf for negative (positive) wind stress curl, as a result of convergent (divergent) Ekman transport (see Li et al., 2019; Pickart et al., 2011).

These results are consistent with the composite map of Figure 16a for the fast period. Included in the figure is the mean wind vector averaged along the coastal pathway (green box in the figure) using the ERA5 reanalysis data. The mean wind was 1.2 m/s out of the east, which, according to Lin et al. (2019), is associated with flow into Barrow Canyon along the coastal pathway. We also show the mean wind stress curl for the fast period (color shading in the figure), which indicates that the curl was generally negative over the northeast part of the shelf. This in turn would favor anti-cyclonic flow around the north and east sides of Hanna Shoal, as observed.

The situation is more complex for the slow period (December to March). The reason for this is that the winds were both stronger and more variable during the winter months of our study year. In contrast to the summer months, there were numerous instances of northeasterly wind, which would be expected to reverse the coastal flow (see also Danielson et al., 2017; Fang et al., 2020; Weingartner, Potter, et al., 2017). The wind stress curl, however, was less variable during this time period, implying that the interior flow should remain largely consistent. For this reason, we computed a single composite for the moorings away from the coast in the general vicinity of Hanna Shoal. To determine which sites to include in this composite, we made a current rose plot for each mooring for the four-month period. Those sites where the flow was consistently in one direction were included in the single composite, which is presented in Figures 16b and 16c. This shows generally cyclonic flow around the east and north sides of Hanna Shoal, which is expected because the wind stress curl was positive in this region. One sees that the flow through Central Channel and northwest of Hanna Shoal is moving in a similar direction as for the fast composite (compare Figures 16a–16c). This is also consistent with the results of Lin et al. (2019) who found that the flow in this region was not as sensitive to the wind stress curl. That is, for both signs of the wind stress curl the flow was northward through Central Channel, bending to the northeast as it exited the channel. This resulted in a region of flow convergence northwest of Hanna Shoal for the positive wind stress curl case (Lin et al., 2019). Such a convergence is evident in Figures 16b and 16c.

For the coastal domain, we made two composites corresponding to the winter period: times when the flow in the coastal pathway was reversed and times when it was not (Figures 16b and 16c, where each composite accounted for roughly half of the 4-month period). This shows two vastly different scenarios. In the case when then the coastal current is flowing in its normal direction, the mean wind is very weak and the flow speeds are considerable (similar to the fast period, compare Figures 16b and 16a). By contrast, when the coastal flow is reversed the speeds are quite large. As expected, the winds are out of the northeast during these conditions. This is consistent with previous studies demonstrating that the alongcoast wind threshold for upwelling (and reversed flow) in Barrow Canyon is 5–6 m/s (Fang et al., 2017; Pisareva et al., 2019; Weingartner et al., 1998).

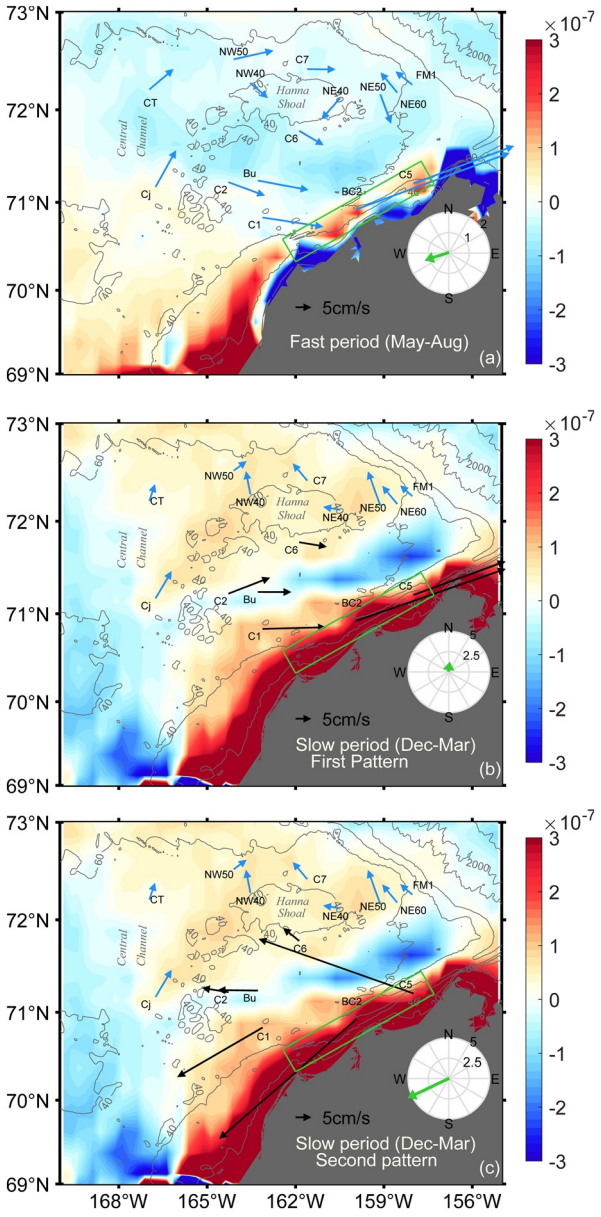

Figure 16. (a) Composite flow pattern during the fast period, from May to August. The blue vectors are the depth-averaged time mean velocity over this time period, and the color is the time mean wind stress curl (N/m^3). The time-mean wind averaged over the green box is shown in the embedded plot. (b) First pattern of flow during the slow period (December to March). The blue vectors in the interior represent the sites that have one dominant direction (same in (c)). The color indicates the wind stress curl (N/m^3) averaged during the slow period (same in (c)). The black arrows are the depth-averaged mean vectors when the coastal flow is to the northeast. The mean wind during these times, averaged over the green box, is shown in the embedded plot. (c) Same as (b) except for the second pattern of flow during the slow period when the coastal flow is reversed. The bathymetry is from IBCAO v3.

Interestingly, the flow at moorings C2, Bu, and C6 is also reversed, even though these moorings are a fair distance from the coast. In the case of C2 and Bu, this is in line with the results of Lin et al. (2019) who found that the flow was directed to the west in this same vicinity when the coastal current was reversed. However, it is not obvious why the flow at C6 reverses in response to the wind. Unfortunately, Lin et al. (2019) have only partial data coverage in this region and hence we are unable to say if our results are consistent with theirs or not. Further work is required to investigate the sensitivity to wind at this location. Although not shown in Figures 16b and 16c, the flow in Bering Strait was northward for both winter composites, which means that, in the case of reversed flow in Barrow Canyon, there is a strong flow convergence somewhere along the coast. This scenario was noted as well in Weingartner et al. (1998). Future work will explore the relationship between the flow in Bering Strait and the circulation on the northeast shelf using our composite data set, although it is unfortunate that mooring SCH had no velocity measurements. Finally, it should be noted that when we construct a single composite of the coastal flow for the winter period, it shows weak mean vectors. This is consistent with our criterion for defining the slow period. However, unlike the rest of the study domain where the flow was consistently weak throughout the winter period, it is the result of strong, oppositely directed flows canceling each other out.

5. Summary

Using timeseries from 20 moorings on the northeastern Chukchi Shelf and in Bering Strait from late-summer 2013 to 2014, aspects of the mean and seasonally varying circulation and hydrography were investigated. The moorings contained near-bottom sensors measuring temperature and salinity, and all but two had upward-facing ADCPs providing vertical profiles of velocity. Averaged over the year-long period, bottom temperatures were warmest in Bering Strait and along the coastal pathway, due to the presence of Alaskan Coastal Water in the warm months of the year. The freshest bottom water was found in Bering Strait for the same reason, but the year-long mean salinities along the coastal pathway were saltier than on the central shelf due to the wintertime presence of polynyas/leads along the coast. The strongest depth-mean flow was in Bering Strait and in the coastal pathway. On the interior shelf the mean flow progresses anti-cyclonically around the north and east sides of Hanna Shoal, a pattern that is more evident in the deep layer. The mean vectors in the warm months of the year are consistent with an independent data set of shipboard ADCP velocities. Together, these show how the Central Channel flow branch bifurcates, with flow around both sides of Hanna Shoal that ultimately drains through Barrow Canyon.

From early winter to early summer, the moorings show a prolonged period with temperature at/near the freezing point (with interruptions associated with short-lived events). At each site, we documented the beginning and end of this period, referred to as the cold water appearance time and warm water appearance time, respectively, with the aim of understanding the nature and timing of these signals, including their relationship to freeze-up and melt-back. Using the measured velocities, it was demonstrated that the warm water appearance times can be linked

to advection along the flow pathways on the eastern Chukchi shelf. The time for warm water to travel from Bering Strait to Barrow Canyon is 2.5–6 months, via the fastest and slowest pathways, respectively.

The cold water appearance times were not reflective of advection, since the cold water shows up in Barrow Canyon before Bering Strait. They are also not simply related to the time of freeze-up throughout the domain. We examined two regions of differing appearance times: (a) the vicinity of 71°N, which is approximately the latitude of Barrow Canyon; and (b) the region extending from south of Hanna Shoal to the northeast. In the former, the cold water appeared in early December around the time of freeze up. The appearance of the cold water was accompanied by a freshening of the bottom water. Using the one-dimensional PWP model, we demonstrated that wind mixing, due to synoptic storm events, was able to overturn the water column during the month preceding the appearance of the cold water. The air-sea heat flux cooled the surface water and the cold temperature signal was mixed to depth. We argue that the freshening was due to the loitering pack ice in the region which, together with the relatively warm southerly winds, would melt ice and provide an intermittent source of fresh water to the region. The PWP model showed that pulsed releases of fresh water at the surface are mixed to depth which leads to freshening in concert with the cooling.

In the second region near Hanna Shoal, the cold water appeared 1–1.5 months later, long after freeze-up, despite comparable wind and heat flux forcing. Using the historical hydrographic data set, we demonstrated that the water column east and south of the shoal in late-summer/early fall is more stratified than anywhere else on the northeast Chukchi shelf. This is due to the presence of a fresh, cold surface layer, which seems to be related to the later melt-back causing fresh water to advect and mix into this region. The one-dimensional mixing model shows that this enhanced stratification prohibits autumn overturning of the water column, which can explain the disparity in cold water appearance times between the two regions. This suggests that the cold water measured in the vicinity of Hanna Shoal is advected from the south under the pack ice.

Finally, we contrasted the flow on the shelf between periods of fast mean flow (May–August) and weak mean flow (December–March). The circulation in the former period is much like the year-long mean flow except stronger. The anti-cyclonic flow around the north and east sides of Hanna Shoal is consistent with the negative wind stress curl on the northeast Chukchi shelf during this period, a result in line with previous studies. By contrast, there are two predominant patterns of flow in the winter period corresponding to different states of the coastal flow. In the first, the coastal flow is to the northeast during periods of weak winds, and, in the second, the coastal flow is reversed to the southwest under strong northeasterly winds. The flow on the interior shelf, however, remains the same in both of these configurations. This is because the wind stress curl is predominantly positive during the winter months, which leads to cyclonic flow around the east and north sides of Hanna Shoal.

Our study can be considered as a companion study to Woodgate et al. (2005a) who analyzed timeseries from a large set of moorings on the Chukchi shelf deployed from autumn 1990 to autumn 1991. In the period studied here, (2013–2014) the flow through Bering Strait was stronger, warmer, and fresher. In addition, the average wind was weaker, the ice-free period was shorter, and coastal polynyas/leads were present more often. However, it is difficult to draw conclusions regarding similarities and differences between the results of the two studies. This is partly because the earlier set of moorings were spread across the Chukchi shelf, whereas the moorings considered here were concentrated mainly in the northeast. Also, the two studies focused on different aspects of the hydrography and circulation. For example, Woodgate et al. (2005a) discussed at length the role of wind forcing on the flow, whereas we spent much effort examining the nature and timing of the temperature signals across the shelf. However, there is some spatial overlap in the mooring coverage, and, as such, it would be fruitful to approach both data sets with a common set of objectives, which is the aim of future work.

Data Availability Statement

The mooring data are available at the following sites: UW moorings A2, A3, and A4: http://psc.apl.washington.edu/HLD/Bstrait/Data/BeringStraitMooringDataArchive.html; JAMSTEC moorings BCH: http://www.jamstec.go.jp/arctic/data_archive_work/mooring/mooring_index.html; WHOI moorings CT: https://www.data.boem.gov/ PMEL mooring C1, C2, C5, C6, and C7: NCEI submittal Reference ID E13NLG, 19RD6Y, 1JC625, H2LC81, UJCDN3, and 5YX626. All other moorings are in NODC (NCEI) archives (https://www.

ncei.noaa.gov/access/metadata/landing-page/bin/iso?id=gov.noaa.nodc:0164964): ASL Moorings Cj and Bu: 0164964 Currents, Ice Analysis, Temperature, and Salinity from Industry Sponsored Moorings in the Chukchi Sea, Alaska, 2008–2016. UAF Mooring BC2: 0160090 Currents, Temperature, Salinity, and Sea Ice measurements from moorings in Barrow Canyon, Chukchi Sea, 2010–2015. UAF Moorings NW40, NW50, NE40, NE50, NE60, FM1: 0163833 Currents, Ice Velocity, Temperature, and Salinity from moorings around Hanna Shoal, Chukchi Sea, 2012–2014.

Acknowledgements
A large number of technicians were responsible for the collection, processing, and quality control of the data that went into this study. The authors are extremely grateful to all of these individuals, and to the funding agencies that supported the respective field programs: The Bureau of Ocean Energy Management; The National Oceanic and Atmospheric Administration; The National Science Foundation; and The Japanese Agency for Marine-Earth Science and Technology. Support for this analysis was provided by the following grants: National Oceanic and Atmospheric Administration grant NA14OAR4320158; National Science Foundation grants PLR-1504333, OPP-1733564, PLR-1758565; North Pacific Research Board grants A91-99a and A91-00a; Chinese Arctic and Antarctic grant CXPT2020009; Natural Sciences and Engineering Research Council of Canada.

References

Aagaard, K., & Roach, A. T. (1990). Arctic ocean-shelf exchange: Measurements in Barrow Canyon. *Journal of Geophysical Research*, *95*(C10), 18163–18175. https://doi.org/10.1029/jc095ic10p18163

Ardyna, M., Babin, M., Gosselin, M., Devred, E., Rainville, L., & Tremblay, J.-É. (2014). Recent Arctic Ocean sea ice loss triggers novel fall phytoplankton blooms. *Geophysical Research Letters*, *41*(17), 6207–6212. https://doi.org/10.1002/2014gl061047

Boyer, T. P., Baranova, O. K., Coleman, C., Garcia, H. E., Grodsky, A., Locarnini, R. A., et al. (2018). *World Ocean database 2018*. (in preparation)

Brugler, E. T., Pickart, R. S., Moore, G. W. K., Roberts, S., Weingartner, T. J., & Statscewich, H. (2014). Seasonal to interannual variability of the Pacific water boundary current in the Beaufort Sea. *Progress in Oceanography*, *127*, 1–20. https://doi.org/10.1016/j.pocean.2014.05.002

Coachman, L. K., Coachman, L. K., Aagaard, K., & Tripp, R. B. (1975). *Bering Strait: The regional physical oceanography*. University of Washington Press

Corlett, W. B., & Pickart, R. S. (2017). The Chukchi slope current. *Progress in Oceanography*, *153*, 50–65. https://doi.org/10.1016/j.pocean.2017.04.005

Danielson, S. L., Ahkinga, O., Ashjian, C., Basyuk, E., Cooper, L. W., Eisner, L., et al. (2020). Manifestation and consequences of warming and altered heat fluxes over Bering and Chukchi Sea continental shelves. *Deep Sea Research Part II: Topical Studies in Oceanography*, *177*, 104781. https://doi.org/10.1016/j.dsr2.2020.104781

Danielson, S. L., Eisner, L., Ladd, C., Mordy, C., Sousa, L., & Weingartner, T. J. (2017). A comparison between late summer 2012 and 2013 water masses, macronutrients, and phytoplankton standing crops in the northern Bering and Chukchi Seas. *Deep Sea Research Part II: Topical Studies in Oceanography*, *135*, 7–26. https://doi.org/10.1016/j.dsr2.2016.05.024

Danielson, S. L., Weingartner, T. J., Hedstrom, K. S., Aagaard, K., Woodgate, R., Curchitser, E., & Stabeno, P. J. (2014). Coupled wind-forced controls of the Bering-Chukchi shelf circulation and the Bering Strait throughflow: Ekman transport, continental shelf waves, and variations of the Pacific-Arctic sea surface height gradient. *Progress in Oceanography*, *125*, 40–61. https://doi.org/10.1016/j.pocean.2014.04.006

Fairall, C. W., Bradley, E. F., Hare, J. E., Grachev, A. A., & Edson, J. B. (2003). Bulk parameterization of air-sea fluxes: Updates and verification for the COARE algorithm. *Journal of Climate*, *16*, 571–591. https://doi.org/10.1175/1520-0442(2003)016<0571:bpoasf>2.0.co;2

Fang, Y. C., Potter, R. A., Statscewich, H., Weingartner, T. J., Winsor, P., & Irving, B. K. (2017). Surface current patterns in the northeastern Chukchi Sea and their response to wind forcing. *Journal of Geophysical Research: Oceans*, *122*(12), 9530–9547. https://doi.org/10.1002/2017jc013121

Fang, Y. C., Weingartner, T. J., Dobbins, E. J., Winsor, P., Statscewich, H., Potter, R. A., et al. (2020). Circulation and thermohaline variability of the Hanna Shoal region on the Northeastern Chukchi Sea shelf. *Journal of Geophysical Reasearch: Oceans*, *125*. https://doi.org/10.1029/2019jc015639

Foukal, N. P., Pickart, R. S., Moore, G. W. K., & Lin, P. (2019). Shelfbreak Downwelling in the Alaskan Beaufort Sea. *Journal of Geophysical Research: Oceans*, *124*(10), 7201–7225. https://doi.org/10.1029/2019jc015520

Frey, K. E., Moore, G. W. K., Cooper, L. W., & Grebmeier, J. M. (2015). Divergent patterns of recent sea ice cover across the Bering, Chukchi, and Beaufort seas of the Pacific Arctic Region. *Progress in Oceanography*, *136*, 32–49. https://doi.org/10.1016/j.pocean.2015.05.009

Gill, A. E. (1982). *Atmosphere-ocean dynamics*. San Diego, CA: Academic.

Gong, D., & Pickart, R. S. (2016). Early summer water mass transformation in the eastern Chukchi Sea. *Deep Sea Research Part II: Topical Studies in Oceanography*, *130*, 43–55. https://doi.org/10.1016/j.dsr2.2016.04.015

Hersbach, H., & Dee, D. J. E. N. (2016). ERA5 reanalysis is in production. *ECMWF newsletter*, *147*(7), 5–6.

Hill, V., & Cota, G. (2005). Spatial patterns of primary production on the shelf, slope and basin of the Western Arctic in 2002. *Deep Sea Research Part II: Topical Studies in Oceanography*, *52*(24–26), 3344–3354. https://doi.org/10.1016/j.dsr2.2005.10.001

Hirano, D., Fukamachi, Y., Watanabe, E., Ohshima, K. I., Iwamoto, K., Mahoney, A. R., et al. (2016). A wind-driven, hybrid latent and sensible heat coastal polynya off B arrow, A laska. *Journal of Geophysical Research: Oceans*, *121*(1), 980–997. https://doi.org/10.1002/2015jc011318

Hogg, N. G., Siedler, G., & Zenk, W. (1999). Circulation and Variability at the Southern Boundary of the Brazil Basin. *Journal of Physical Oceanography*, *29*, 145–157. https://doi.org/10.1175/1520-0485(1999)029<0145:cavats>2.0.co;2

Ladd, C., Mordy, C. W., Salo, S. A., & Stabeno, P. J. (2016). Winter water properties and the Chukchi Polynya. *Journal of Geophysical Research: Oceans*, *121*(8), 5516–5534. https://doi.org/10.1002/2016jc011918

Lammers, R. B., Shiklomanov, A. I., Vörösmarty, C. J., Fekete, B. M., & Peterson, B. J. (2001). Assessment of contemporary Arctic river runoff based on observational discharge records. *Journal of Geophysical Research*, *106*(D4), 3321–3334. https://doi.org/10.1029/2000jd900444

Li, M., Pickart, R. S., Spall, M. A., Weingartner, T. J., Lin, P., Moore, G. W. K., & Qi, Y. (2019). Circulation of the Chukchi Sea shelfbreak and slope from moored timeseries. *Progress in Oceanography*, *172*, 14–33. https://doi.org/10.1016/j.pocean.2019.01.002

Lin, P., Pickart, R. S., McRaven, L. T., Arrigo, K. R., Bahr, F., Lowry, K. E., et al. (2019). Water mass evolution and circulation of the northeastern Chukchi Sea in summer: Implications for nutrient distributions. *Journal of Geophysical Research: Oceans*, *124*(7), 4416–4432. https://doi.org/10.1029/2019JC015185

Lin, P., Pickart, R. S., Stafford, K. M., Moore, G. W. K., Torres, D. J., Bahr, F., & Hu, J. (2016). Seasonal variation of the Beaufort shelfbreak jet and its relationship to Arctic cetacean occurrence. *Journal of Geophysical Research: Oceans*, *121*(12), 8434–8454. https://doi.org/10.1002/2016jc011890

Lu, K., Danielson, S., Hedstrom, K., & Weingartner, T. (2020). Assessing the role of oceanic heat fluxes on ice ablation of the central Chukchi Sea Shelf. *Progress in Oceanography*, *184*, 102313. https://doi.org/10.1016/j.pocean.2020.102313

Moore, G. W. K., Våge, K., Pickart, R. S., & Renfrew, I. A. (2015). Decreasing intensity of open-ocean convection in the Greenland and Iceland seas. *Nature Climate Change*, *5*(9), 877–882. https://doi.org/10.1038/nclimate2688

Nikolopoulos, A., Pickart, R. S., Fratantoni, P. S., Shimada, K., Torres, D. J., & Jones, E. P. (2009). The western Arctic boundary current at 152°W: Structure, variability, and transport. *Deep Sea Research Part II: Topical Studies in Oceanography*, *56*(17), 1164–1181. https://doi.org/10.1016/j.dsr2.2008.10.014

Pacini, A., Moore, G. W. K., Pickart, R. S., Nobre, C., Bahr, F., Våge, K., & Arrigo, K. R. (2019). Characteristics and transformation of Pacific winter water on the Chukchi Sea shelf in late spring. *Journal of Geophysical Research: Oceans*, *124*, 7153–7177. https://doi.org/10.1029/2019jc015261

Paquette, R. A., & Bourke, R. H. (1974). Observations on the coastal current of Arctic Alaska. *Journal of Marine Research*, *32*(2), 195–207.

Pawlowicz, R., Beardsley, B., & Lentz, S. (2002). Classical tidal harmonic analysis including error estimates in MATLAB using T_TIDE. *Computers & Geosciences*, *28*(8), 929–937. https://doi.org/10.1016/s0098-3004(02)00013-4

Pickart, R. S. (2004). Shelfbreak circulation in the Alaskan Beaufort Sea: Mean structure and variability. *Journal of Geophysical Research*, *109*(C4). https://doi.org/10.1029/2003jc001912

Pickart, R. S., Moore, G. W. K., Mao, C., Bahr, F., Nobre, C., & Weingartner, T. J. (2016). Circulation of winter water on the Chukchi shelf in early Summer. *Deep Sea Research Part II: Topical Studies in Oceanography*, *130*, 56–75. https://doi.org/10.1016/j.dsr2.2016.05.001

Pickart, R. S., Pratt, L. J., Torres, D. J., Whitledge, T. E., Proshutinsky, A. Y., Aagaard, K., et al. (2010). Evolution and dynamics of the flow through Herald Canyon in the western Chukchi Sea. *Deep Sea Research Part II: Topical Studies in Oceanography*, *57*(1–2), 5–26. https://doi.org/10.1016/j.dsr2.2009.08.002

Pickart, R. S., Schulze, L. M., Moore, G. W. K., Charette, M. A., Arrigo, K. R., van Dijken, G., & Danielson, S. L. (2013). Long-term trends of upwelling and impacts on primary productivity in the Alaskan Beaufort Sea. *Deep Sea Research Part I: Oceanographic Research Papers*, *79*, 106–121. https://doi.org/10.1016/j.dsr.2013.05.003

Pickart, R. S., Spall, M. A., Moore, G. W. K., Weingartner, T. J., Woodgate, R. A., Aagaard, K., & Shimada, K. (2011). Upwelling in the Alaskan Beaufort Sea: Atmospheric forcing and local versus non-local response. *Progress in Oceanography*, *88*, 78–100. https://doi.org/10.1016/j.pocean.2010.11.005

Pisareva, M. N., Pickart, R. S., Lin, P., Fratantoni, P. S., & Weingartner, T. J. (2019). On the nature of wind-forced upwelling in Barrow Canyon. *Deep Sea Research Part II: Topical Studies in Oceanography*, *162*, 63–78. https://doi.org/10.1016/j.dsr2.2019.02.002

Pisareva, M. N., Pickart, R. S., Spall, M. A., Nobre, C., Torres, D. J., Moore, G. W. K., & Whitledge, T. E. (2015). Flow of Pacific water in the western Chukchi Sea: Results from the 2009 RUSALCA expedition. *Deep Sea Research Part I: Oceanographic Research Papers*, *105*, 53–73. https://doi.org/10.1016/j.dsr.2015.08.011

Price, J. F., Weller, R. A., & Pinkel, R. (1986). Diurnal cycling: Observations and models of the upper ocean response to diurnal heating, cooling, and wind mixing. *Journal of Geophysical Research*, *91*(C7), 8411–8427. https://doi.org/10.1029/jc091ic07p08411

Proshutinsky, A., Krishfield, R., Timmermans, M. L., Toole, J., Carmack, E., McLaughlin, F., et al. (2009). Beaufort Gyre freshwater reservoir: State and variability from observations. *Journal of Geophysical Research*, *114*(C1). https://doi.org/10.1029/2008jc005104

Roach, A. T., Aagaard, K., Pease, C. H., Salo, S. A., Weingartner, T., Pavlov, V., & Kulakov, M. (1995). Direct measurements of transport and water properties through the Bering Strait. *Journal of Geophysical Research*, *100*(C9), 18443–18457. https://doi.org/10.1029/95jc01673

Shimada, K., Kamoshida, T., Itoh, M., Nishino, S., Carmack, E., McLaughlin, F., et al. (2006). Pacific Ocean inflow: Influence on catastrophic reduction of sea ice cover in the Arctic Ocean. *Geophysical Research Letters*, *33*(8). https://doi.org/10.1029/2005gl025624

Shroyer, E. L., & Pickart, R. S. (2019). Pathways, timing, and evolution of Pacific winter water through Barrow canyon. *Deep sea Research, Part II: Topical Studies in oceanography*, *162*, 50–62. https://doi.org/10.1016/j.dsr2.2018.05.004

Spall, M. A. (2007). Circulation and water mass transformation in a model of the Chukchi Sea. *Journal of Geophysical Research*, *112*(C5). https://doi.org/10.1029/2005jc003364

Stabeno, P., Kachel, N., Ladd, C., & Woodgate, R. (2018). Flow Patterns in the Eastern Chukchi Sea: 2010–2015. *Journal of Geophysical Research: Oceans*, *123*(2), 1177–1195. https://doi.org/10.1002/2017jc013135

Våge, K., Pickart, R. S., Spall, M. A., Moore, G. W. K., Valdimarsson, H., Torres, D. J., et al. (2013). Revised circulation scheme north of the Denmark Strait. *Deep Sea Research Part I: Oceanographic Research Papers*, *79*, 20–39. https://doi.org/10.1016/j.dsr.2013.05.007

Weingartner, T. J., Aagaard, K., Woodgate, R., Danielson, S., Sasaki, Y., & Cavalieri, D. (2005). Circulation on the north central Chukchi Sea shelf. *Deep Sea Research Part II: Topical Studies in Oceanography*, *52*(24–26), 3150–3174. https://doi.org/10.1016/j.dsr2.2005.10.015

Weingartner, T. J., Cavalieri, D. J., Aagaard, K., & Sasaki, Y. (1998). Circulation, dense water formation, and outflow on the northeast Chukchi shelf. *Journal of Geophysical Research*, *103*(C4), 7647–7661. https://doi.org/10.1029/98jc00374

Weingartner, T. J., Fang, Y.-C., Winsor, P., Dobbins, E., Potter, R., Statscewich, H., et al. (2017). The summer hydrographic structure of the Hanna Shoal region on the northeastern Chukchi Sea shelf: 2011–2013. *Deep Sea Research Part II: Topical Studies in Oceanography*, *144*, 6–20. https://doi.org/10.1016/j.dsr2.2017.08.006

Weingartner, T. J., Potter, R. A., Stoudt, C. A., Dobbins, E. L., Statscewich, H., Winsor, P. R., et al. (2017). Transport and thermohaline variability in Barrow Canyon on the Northeastern Chukchi Sea Shelf. *Journal of Geophysical Research: Oceans*, *122*, 3565–3585. https://doi.org/10.1002/2016JC012636

Winsor, P., & Chapman, D. C. (2004). Pathways of Pacific water across the Chukchi Sea: A numerical model study. *Journal of Geophysical Research*, *109*(C3). https://doi.org/10.1029/2003jc001962

Wiseman, W. J., Jr, & Rouse, L. J., Jr (1980). A coastal jet in the Chukchi Sea. *Arctic*, *33*(1), 21–29. https://www.jstor.org/stable/40509272

Woodgate, R. A. (2018). Increases in the Pacific inflow to the Arctic from 1990 to 2015, and insights into seasonal trends and driving mechanisms from year-round Bering Strait mooring data. *Progress in Oceanography*, *160*, 124–154. https://doi.org/10.1016/j.pocean.2017.12.007

Woodgate, R. A., Aagaard, K., & Weingartner, T. J. (2005). A year in the physical oceanography of the Chukchi Sea: Moored measurements from autumn 1990–1991. *Deep Sea Research Part II: Topical Studies in Oceanography*, *52*(24–26), 3116–3149. https://doi.org/10.1016/j.dsr2.2005.10.016

Woodgate, R. A., Aagaard, K., & Weingartner, T. J. (2005). Monthly temperature, salinity, and transport variability of Bering Strait through flow. *Geophysical Research Letters*, *32*(4). https://doi.org/10.1029/2004gl021880

Woodgate, R. A., Stafford, K., & Prahl, F. (2015). A synthesis of year-round interdisciplinary Mooring measurements in the Bering Strait (1990-2014) and the RUSALCA years (2004-2011). *Oceanography*, *28*(3), 46–67. https://doi.org/10.5670/oceanog.2015.5710.5670/oceanog.2015.57

Woodgate, R. A., Weingartner, T. J., & Lindsay, R. (2012). Observed increases in Bering Strait oceanic fluxes from the Pacific to the Arctic from 2001 to 2011 and their impacts on the Arctic Ocean water column. *Geophysical Research Letters*, *39*(24). https://doi.org/10.1029/2012GL054092

Woodgate, R. A., Weingartner, T., & Lindsay, R. (2010). The 2007 Bering Strait oceanic heat flux and anomalous Arctic sea-ice retreat. *Geophysical Research Letters*, *37*(1), a–n. https://doi.org/10.1029/2009GL041621

Yang, J. (2006). The seasonal variability of the Arctic Ocean Ekman transport and its role in the mixed layer heat and salt fluxes. *Journal of Climate*, *19*(20), 5366–5387. https://doi.org/10.1175/jcli3892.1

Zhang, J., Woodgate, R., & Moritz, R. (2010). Sea ice response to atmospheric and oceanic forcing in the Bering Sea. *Journal of physical oceanography*, *40*(8), 1729–1747. https://doi.org/10.1175/2010JPO4323.1